

Transfer learning based physics-informed neural networks for solving inverse problems in tunneling

Chen Xu^a, Ba Trung Cao^a, Yong Yuan^b, Günther Meschke^{a,1,*}

^a*Institute for Structural Mechanics, Ruhr-University Bochum, Universitätsstraße 150, 44801 Bochum, Germany*

^b*Department of Geotechnical Engineering, College of Civil Engineering, Tongji University, 1239 Siping Road, 20092 Shanghai, China*

Abstract

Recently, a class of machine learning methods called physics-informed neural networks (PINNs) has been proposed and gained great prevalence in solving various scientific computing problems. This approach enables the solution of partial differential equations (PDEs) via embedding physical laws into the loss function of neural networks. Many inverse problems can also be tackled by simply combining the observational data from real life scenarios with existing PINN algorithms. In this paper, we present a multi-task learning method to improve the training stability of PINNs for linear elastic problems, and the homoscedastic uncertainty is introduced as a basis for weighting losses. Furthermore, we demonstrate an application of PINNs to a practical inverse problem in tunnel engineering: prediction of external loading distributions of tunnel rings based on a limited number of displacement monitoring points. To this end, we first determine a simplified tunneling scenario at the offline stage. By setting unknown boundary conditions as learnable parameters, PINNs can predict the external loads applied on the tunnel lining with the support of enough measurement data. When it comes to the online stage in real tunnel projects, the Kriging method is adopted to reconstruct the whole displacement field based on very limited measurements. Then transfer learning is employed to fine-tune the pre-trained model from offline stage. Our results show that, although the reconstructed displacement field generated from gappy measurements is accompanied by errors, satisfactory results can still be obtained from the PINN model due to the dual regularization of physics laws and prior knowledge, which exhibits better robustness compared to traditional analysis methods. The convergence of training is also accelerated, thus making it possible for PINNs to be applied in actual tunnel projects.

Keywords: Physics-informed neural networks (PINNs), Multi-task learning, Transfer learning, Kriging method, Inverse analysis, Tunnel engineering

*Corresponding author

¹email: guenther.meschke@rub.de

1. Introduction

Growing population, urbanization and the need for high-speed mobility has increased the necessity for underground transportation systems in modern era. In recent years, a large number of tunnels has been constructed to improve existing transportation systems. Within a tunnel, the main structure, i.e. the tunnel lining, is designed to permanently fulfill basic structural, serviceability and durability requirements during the lifetime of the tunnel. To ensure the structural stability, it is essential to correctly assess and evaluate the response of the tunnel lining, which requires a proper quantification of loading scenarios acting on the lining, including the distribution and magnitude. Different methods have been proposed to directly identify the lining internal forces or the surrounding loads from displacement measurements at construction sites. In [1, 2, 3], histories of in-situ displacement fields are combined with non-linear finite element analyses in a hybrid combination concept to quantify for the loading situation on shotcrete shells, which were used as the tunnel lining in the New Austrian Tunneling Method. The hybrid analysis is also validated using monitored displacement from a full-scale test of a segmented tunnel ring [4]. Alternatively, bending moments and axial forces of piles, retaining walls and tunnel structures can be obtained from an analytical solution based on the principle of virtual work using displacement measurements [5]. Another analytical solution based on the theory of a circular curved beam were also utilized to provide the internal forces of primary support in deep tunnels [6]. Within the back-analysis method, on-site radial displacements of primary linings and contact stresses between shotcrete and surrounding rocks are used to estimate the structural behavior of a symmetrically loaded tunnel. Recently, a new method employed in tunnel inspection, i.e. the laser scanning, is employed together with a displacement-based hybrid structural analysis to predict internal forces of segmental linings [7]. Within the hybrid analysis, a finite element method (FEM) model for the segmental lining ring is coupled with displacement field in a displacement-controlled FEM analysis to estimate bending moments and axial forces of the lining ring. The above-mentioned works show a great potential of characterizing the structural behavior of the tunnel lining by means of exploiting measured data of the on-site displacements and a proper computational analysis tool. In this paper, we propose an approach for solving the inverse problem to quantify for the external loads acting on circular continuous tunnel linings. The adopted approach is the combination of available displacement measurements at a limited number of monitoring locations around the lining and a computational model based on a recently developed class of machine learning, called physics-informed neural networks (PINNs).

Machine learning has continued its forward movement over the past few years with advances in many exciting research areas, especially the branch of deep learning [8], which is attributed to massive accumulation of data, advanced algorithms and availability of high performance computing. Meanwhile, an increasing number of applications of deep learning has been witnessed in the field of computational mechanics and engineering, e.g. fluid mechanics [9, 10], molecular dynamics [11, 12], learning constitutive laws [13, 14, 15], solving fracture problems [16, 17], material property prediction [18, 19, 20], surrogate modeling [21, 22, 23], model order reduction [24, 25] and multi-scale analysis [26, 27, 28, 29],

to name a few examples. However, in most of these methods, a large amount of data collected from laboratory experiments or high-fidelity numerical simulations is inevitably required to establish a database for supervised learning. Neural networks (NN) can then be treated as a "black box" to accomplish the nonlinear mapping between inputs and outputs. The robustness of NN highly depends on the noise level of experimental data, the accuracy of numerical simulations and the volume of accumulated data.

Recently, a different class of NNs known as physics-informed neural networks was introduced [30, 31] and has already gained a lot of attention in the scientific machine learning community. As a promising alternative of numerical discretization schemes, PINNs can solve partial differential equations (PDEs) by embedding the physical description (e.g. laws of physics and constraints) into deep learning, without the requirement for big data as mentioned above. The built-in physical constraints inherently give rise to clearer interpretability with physics meaning for NNs. PINNs can leverage current domain knowledge and integrate seamlessly observational data and mathematical models (even those with imperfection), which are effective and efficient for both forward and inverse problems. As the pioneer in this research field, Karniadakis's research team has already extended PINNs into different versions, such as P-PINN for time-dependent PDEs [32], C-PINNs on discrete domains for conservation laws [33], N-PINNs for non-local models [34], hp-VPINNs with hp-refinement for function approximation [35], and B-PINNs for uncertainty quantification [36].

The original network architecture of PINNs can be replaced flexibly for solving various problems. For instance, physics-informed convolutional neural networks (CNNs) was proposed to learn solutions of parametric PDEs on irregular domains [37]. If incorporating physics knowledge into long short-term memory (LSTM) networks, sequence-to-sequence features could be accurately captured, thus enabling the prediction of seismic responses of nonlinear structural systems [38]. The physics-informed generative adversarial networks (PI-GANs) developed in [39] can solve stochastic differential equations (SDEs) based on a limited number of scattered measurements. The PINN framework based on graph convolutional network (GCN) [40] can strictly impose hard boundary conditions and handle irregular domains with unstructured meshes. Up to now, PINNs have been successfully applied to a wide range of scientific problems, e.g. fluid mechanics [41, 42, 43, 44, 45], additive manufacturing [46, 47], cardiovascular flows modeling [48], subsurface flow prediction [49] and reservoir simulation [50]. Several open source libraries such as DeepXDE [51], SimNet [52] and SciANN [53] were also developed to bridge the gap between PINN theory and its practical application. It is worth noting that PINN models sometimes suffer from training failures (e.g. slow convergence rate and bad minima), some remedies were thus proposed to resolve these difficulties. Wang et al. [54, 55] investigated the influence of different loss components on the convergence rate through the lens of the Neural Tangent Kernel (NTK), which may shed light on the training dynamics of PINNs. The adaptive activation function employed in [56] has better learning capabilities than the traditional one as it improves greatly the convergence rate as well as the prediction accuracy. Importance sampling approach mentioned in [57] can foster efficient training of PINNs by sampling the collocation points according to a distribution proportional to the loss function.

The emergence of physics-informed machine learning has brought new hopes to addressing solid mechanics problems in a different way. Haghighat et al. [58] presented the application of PINNs to learning and discovery in solid mechanics, specifically linear elasticity and elasto-plasticity. A multi-network model was proposed to boost the training speed, and the transfer learning was also implemented to accelerate re-training process, which has a great potential for sensitivity analysis. Moreover, they developed a nonlocal PINN approach using the Peridynamic Differential Operator (PDDO) [59]. By incorporating long-range interactions and removing spatial derivatives in the governing PDEs, this method can better capture the solution with sharp gradients. Inspired by the variational formulation of PDEs, Samaniego et al. [60] proposed the deep energy method (DEM) and rewrote the loss function of PINN as the potential energy of the system. The gradient descent of loss function during NN optimization procedure naturally satisfies the goal of minimum total potential energy principle, which opens a door to its application to various mechanical problems by defining the corresponding energies [61]. A more comprehensive comparison of governing equation-based (original PINNs) and energy-based (DEM) approaches can be referred to in [62]. Inspired by classical FEMs where basis functions are defined piece-wise over sub-regions (i.e. finite elements) and each basis function has compact support over an element, Moseley et al. [63] proposed a new domain decomposition approach for PINNs called Finite Basis PINNs (FBPINNs), which are effective in solving problems with large domains and multi-scale solutions.

Most of the existing papers focus on the application of PINNs to various forward problems, i.e. PINN is treated as a meshless numerical solver for partial differential equations. Despite that switching from numerical discretization schemes to mathematical optimization is promising, in terms of computational cost and accuracy, PINN still cannot outperform traditional computational methods such as FEMs. Therefore, in this paper, we exploit one of the best features of PINN, i.e. integration of observational data and physics models, to solve the aforementioned inverse problem in tunnel engineering. Since the unbalanced back-propagated gradients during network training will pose a great challenge to the convergence of PINNs [64], some multi-task optimization methods are employed to mitigate the balance conflicts among different loss terms, e.g. Gradient Surgery in [65] and GradNorm in [66]. In this paper, we first non-dimensionalize governing equations of linear elasticity, and a multi-task learning method using homoscedastic uncertainty [67] is then introduced to allocate relative weightings to different learning objectives, which enhances the accuracy of PINN and successfully gets validation through a benchmark problem. By directly setting the boundary conditions as learnable parameters, PINN can accurately predict the surrounding pressure around the tunnel if supported by a sufficient amount of monitoring data. Usually, it is difficult to obtain point cloud data of structural deformations in actual tunnel projects. Therefore, Kriging, a classical spatial interpolation algorithm, is adopted to acquire enough training data of the whole displacement field based on a limited number of monitoring points. The reconstructed field usually has errors which tend to make PINNs converge to an inaccurate solution, the transfer learning is thus introduced to fine-tune the neural network parameters on the basis of the pre-trained model prepared at the offline stage. Sufficiently accurate prediction results can be obtained with less computational

cost, exhibiting great potential in large-scale inverse analysis of multiple cross-sections in tunneling.

The remainder of this paper is organized as follows: In Section 2, a transfer learning based boundary-condition-learnable physics-informed neural networks is developed. Numerical results showcasing applications of the proposed approach to inverse analysis of tunnel structures are presented in Section 3. Finally, concluding remarks are given in Section 4.

2. Methodology

2.1. PINNs: Physics-informed neural networks

The general form of differential equations can be expressed as:

$$\begin{aligned}\mathcal{D}[\mathbf{u}(\mathbf{x})] &= h(\mathbf{x}), \mathbf{x} \in \Omega, \\ \mathcal{B}[\mathbf{u}(\mathbf{x})] &= g(\mathbf{x}), \mathbf{x} \in \partial\Omega.\end{aligned}\tag{1}$$

Here, $\mathcal{D}[\cdot]$ denotes a differential operator acting on a function \mathbf{u} (i.e. the solution to the differential equation), $\mathcal{B}[\cdot]$ are boundary operators, \mathbf{x} is an input vector in the domain Ω , and $\partial\Omega$ stands for the boundary of Ω . This general formulation can be extended to foundational equations for a wide spectrum of engineering problems, such as thermodynamics, fluid dynamics, and elasticity.

Let us consider a fully connected feed-forward neural network $NN(\mathbf{x}; \theta)$ with input vector \mathbf{x} , output vector \mathbf{u} , and network parameters θ . This L -layer neural network, composed of an input layer, an output layer, and $L - 2$ hidden layers, can approximate the solution function $\mathbf{u}(\mathbf{x})$ through the following function composition:

$$\begin{aligned}\mathbf{u}(\mathbf{x}) &\approx NN(\mathbf{x}; \theta) = f_L \circ \phi \circ f_{L-1} \circ \phi \circ f_{L-2} \circ \phi \cdots \phi \circ f_1(\mathbf{x}), \\ f_l(\mathbf{a}) &= \mathbf{W}_l \cdot \mathbf{a} + \mathbf{b}_l, \quad l = 1, \dots, L,\end{aligned}\tag{2}$$

where ϕ is called activation function and directly determines the nonlinear property of the network. f_l is a transformation function acting on the vector \mathbf{a} . The notation \circ denotes function composition. $\mathbf{W}_l, \mathbf{b}_l$ are parameters between layers, known as weights and biases respectively, which constitute the set of trainable parameters θ .

Given the architecture of a NN, a loss function should be chosen to measure the difference between prediction results obtained from NN and the actual values. In PINN models, loss functions are selected in the following form based on the definition in Eq. (1):

$$\begin{aligned}\mathcal{L}(\theta) &= \mathcal{L}_{PDEs}(\theta) + \mathcal{L}_{BCs}(\theta), \\ \mathcal{L}_{PDEs}(\theta) &= \frac{1}{N_p} \sum_i^{N_p} \|\mathcal{D}[NN(\mathbf{x}_i; \theta)] - h(\mathbf{x})\|^2, \\ \mathcal{L}_{BCs}(\theta) &= \frac{1}{N_{bc}} \sum_j^{N_{bc}} \|\mathcal{B}[NN(\mathbf{x}_j; \theta)] - g(\mathbf{x})\|^2,\end{aligned}\tag{3}$$

here $\mathcal{L}_{PDEs}(\theta)$ indicates the loss related to the PDEs, i.e. the embedded physical description, $\mathcal{L}_{BCs}(\theta)$ represents the loss related to the boundary conditions, $\{\mathbf{x}_i\}$ is a set of training points sampled over the whole domain Ω ($i = 1, 2, \dots, N_p$) and $\{\mathbf{x}_j\}$ is a set of training points sampled from the domain boundary $\partial\Omega$ ($j = 1, 2, \dots, N_{bc}$). Finally, the optimal network parameters θ^* can be obtained by minimizing the loss function $\mathcal{L}(\theta)$. Note that while constructing the term $\mathcal{D}[NN(\mathbf{x}_i; \theta)]$, the derivatives of outputs with respect to inputs can be obtained during back-propagation through the automatic differentiation (AD) module of Pytorch [68]. Based on the chain rule, AD can compute derivatives of arbitrary order automatically, accurately to working precision. Overall, the complete process of a PINN method is depicted in Fig. 1.

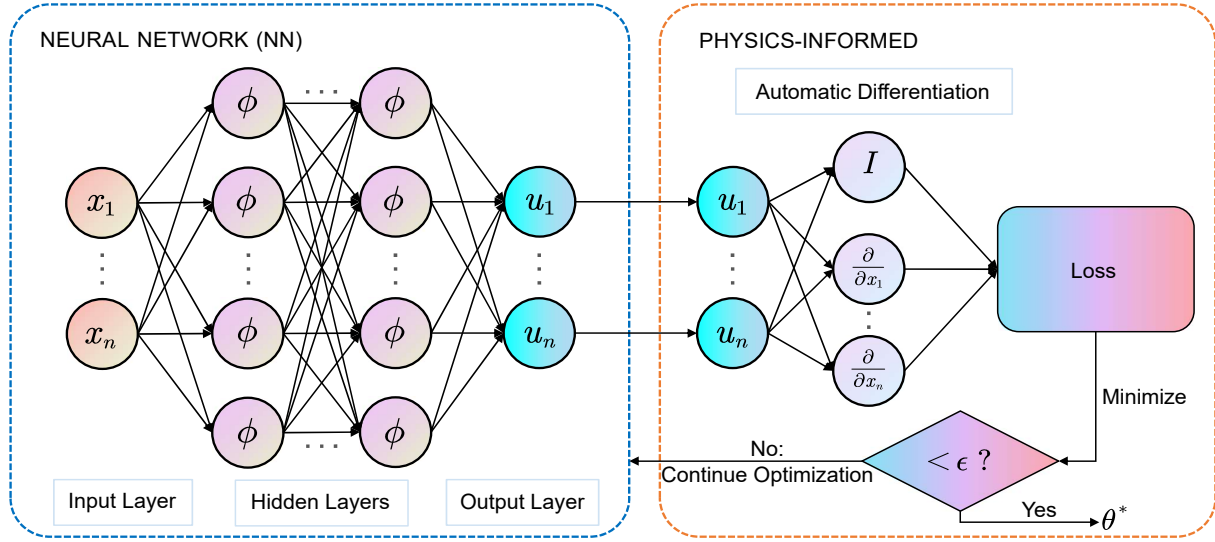


Figure 1: Flowchart of a physics-informed neural network (PINN) framework

2.2. Elasticity with non-dimensionalization

For linear elasticity, the following PDE expresses the momentum balance equation, the constitutive relationship and the kinematic relations under the assumption of small deformation:

$$\rho \frac{\partial^2 u}{\partial t^2} = \nabla((\lambda + \mu)\nabla \cdot u) + \nabla \cdot (\mu \nabla u) + \rho t, \quad (4)$$

where u denotes the displacement vector, ρ represents the density of the material, λ and μ are the Lamé elasticity parameters, and t is a body force. In this paper, all the models involve static or quasi-static deformations where the acceleration term $\rho \frac{\partial^2 u}{\partial t^2}$ is neglected, and the body force t is also absent. In that case,

$$0 = \nabla((\lambda + \mu)\nabla \cdot u) + \nabla \cdot (\mu \nabla u). \quad (5)$$

As mentioned in [69], models in solid mechanics are almost never non-dimensionalized, but our subsequent results in 3.1 will show its effectiveness. We introduce the following

dimensionless variables with scaling factors u_c and l_c :

$$\bar{u} = \frac{u}{u_c}, \quad \bar{x} = \frac{x}{l_c}, \quad \bar{y} = \frac{y}{l_c}, \quad \bar{z} = \frac{z}{l_c}. \quad (6)$$

Inserting the dimensionless variables gives:

$$0 = l_c^{-2} u_c \bar{\nabla} \cdot ((\lambda + \mu) \bar{\nabla} \cdot \bar{u}) + l_c^{-2} u_c \mu \bar{\nabla} \cdot (\bar{\nabla} \bar{u}). \quad (7)$$

Dividing by $l_c^{-2} u_c \mu$ leads to:

$$0 = \bar{\nabla} \cdot ((\delta + 1) \bar{\nabla} \cdot \bar{u}) + \bar{\nabla} \cdot (\bar{\nabla} \bar{u}). \quad (8)$$

Here the dimensionless parameter δ is defined as:

$$\delta = \frac{\lambda}{\mu}. \quad (9)$$

The stress tensor σ is computed by:

$$\sigma = \lambda \text{tr}(\epsilon) I + 2\mu \epsilon = \lambda \nabla \cdot u I + \mu (\nabla u + (\nabla u)^T). \quad (10)$$

With the dimensionless variables, Eq. (10) becomes:

$$\sigma = \lambda u_c l_c^{-1} \bar{\nabla} \cdot \bar{u} + \mu u_c l_c^{-1} (\bar{\nabla} \bar{u} + (\bar{\nabla} \bar{u})^T). \quad (11)$$

By defining the scaling factor σ_c as:

$$\sigma_c = \mu u_c l_c^{-1}, \quad (12)$$

we then can finally get the dimensionless stress tensor:

$$\bar{\sigma} = \frac{\sigma}{\sigma_c} = \bar{\sigma} = \delta \bar{\nabla} \cdot \bar{u} + (\bar{\nabla} \bar{u} + (\bar{\nabla} \bar{u})^T). \quad (13)$$

2.3. Multi-task learning using uncertainty

As mentioned in Section 1, we adopt the multi-task learning method in [67] to weigh the losses for each individual task. It is reported that the homoscedastic uncertainty in Bayesian modeling can capture the relative confidence between tasks, which can thus be described as task-dependent uncertainty for weighting losses. We define the Gaussian likelihood p with mean given by the network output:

$$p(\mathbf{u} \mid NN(\mathbf{x}; \theta)) = \mathcal{N}(NN(\mathbf{x}; \theta), \alpha^2), \quad (14)$$

with the scalar α as a noise parameter. In a setting of a neural network with K tasks, the multi-objective likelihood can be written as:

$$p(\mathbf{u}_1, \dots, \mathbf{u}_K \mid NN(\mathbf{x}; \theta)) = p(\mathbf{u}_1 \mid NN(\mathbf{x}; \theta)) \dots p(\mathbf{u}_K \mid NN(\mathbf{x}; \theta)). \quad (15)$$

In maximum likelihood estimation (MLE), it is often convenient to work with the natural logarithm of the likelihood function, and we can therefore maximize:

$$\begin{aligned}
\log p(\mathbf{u}_1, \dots, \mathbf{u}_K \mid NN(\mathbf{x}; \theta)) &= \log p(\mathbf{u}_1 \mid NN(\mathbf{x}; \theta)) + \dots + \log p(\mathbf{u}_K \mid NN(\mathbf{x}; \theta)) \\
&= \log \mathcal{N}(\mathbf{u}_1; NN(\mathbf{x}; \theta), \alpha_1^2) + \dots + \log \mathcal{N}(\mathbf{u}_K; NN(\mathbf{x}; \theta), \alpha_K^2) \\
&= \left(-\frac{1}{2\alpha_1^2} \mathcal{L}_1 - \log(1 + \alpha_1^2)\right) + \dots + \left(-\frac{1}{2\alpha_K^2} \mathcal{L}_K - \log(1 + \alpha_K^2)\right).
\end{aligned} \tag{16}$$

This leads to our final minimisation target:

$$\mathcal{L}(\theta, \alpha_1, \dots, \alpha_K) = \sum_i^K \left(\frac{1}{2\alpha_i^2} \mathcal{L}_i + \log(1 + \alpha_i^2)\right), \tag{17}$$

where \mathcal{L}_i is the loss related to task i , and the trainable parameters are also extended to include the noise parameter (i.e. task weight) α .

2.4. Kriging method

Kriging is a powerful statistical tool with applications in many fields such as geology, fluid mechanics, process engineering, environment and meteorology. In geology and tunneling, the method, which is also known as a form of probabilistic and local interpolation, is commonly used to estimate the values in unknown areas based on known values of a limited number of nearby geographic areas [70, 71, 72]. Inspired by the characteristic of the Kriging method, the complete displacement field of a tunnel lining can be reconstructed from a limited number of displacement measurements around the lining. Basically, Kriging is an unbiased multi-step procedure which combines known values and a variogram to determine unknown values. Optimal weights obtained from the variogram are assigned to known values in order to compute the data at unknown points. Furthermore, the technique considers both the distance and the degree of variation between known data points when estimating values in unknown areas.

At the first step, the method starts with the exploratory statistical analysis of the data and the generation of an appropriate variogram. The available data is utilized to construct an empirical variogram, which is then fitted numerically to a variogram model. The empirical variogram is calculated by averaging one half the difference squared of the values over all pairs of known data with the specified separation distance between points d and a possible direction following Eq. (18).

$$\gamma(d_x) = \frac{1}{2N(d_x)} \sum_{(i,j) \in N(d_x)} (q_i - q_j)^2. \tag{18}$$

In Eq. (18), γ is called the variance of the variogram; $N(d_x)$ is the number of pairs between data points satisfying the separation distance d following the x direction. The corresponding parameter values at two arbitrary points in this set are denoted as q_i and q_j .

The empirical variogram is then approximated by a functional variogram model, which is usually chosen from a set of mathematical functions describing the spatial relationship. The appropriate model is selected by matching the shape of the curve of the empirical variogram to the shape of the curve of the mathematical function. Exponential, polynomial and Gaussian variogram models are commonly used in geotechnics and tunneling applications. As a result, each known point is given a weight coefficient, which will be used to estimate the value $q(x_0)$ at an arbitrary point x_0 as

$$q(x_0) = \sum_{k=1}^N \eta_k q(x_k). \quad (19)$$

In Eq.(19), $q(x_k)$ represents for the measured values at the k th known location following the x direction. The assigned weight from the variogram model, the number of known data points are symbolized as η and N , respectively. More details about the well-known method Kriging can be found in [73, 74].

2.5. Proposed approach: Transfer learning based boundary-condition-learnable PINNs

In this paper, the neural networks in all cases are composed of five hidden layers with the mostly used hyperbolic tangent activation function (tanh) and each layer has 30 neurons. The non-dimensionalized Cartesian coordinates $\{\bar{x}, \bar{y}, \bar{z}\}$ ($\{\bar{x}, \bar{y}\}$ for 2D problems) are considered as input layer while non-dimensionalized displacements $\{\bar{u}_x, \bar{u}_y, \bar{u}_z\}$ ($\{\bar{u}_x, \bar{u}_y\}$ for 2D problems) are taken as output layer. Consider a set of collocation training points $\{\mathbf{x}_i^{col}\}_{i=1}^{N_{col}}$, free boundary condition points $\{\mathbf{x}_i^{freebc}\}_{i=1}^{N_{freebc}}$, Neumann boundary condition points $\{\mathbf{x}_i^{nbcj}\}_{i=1}^{N_{nbcj}}$, Dirichlet boundary condition points $\{\mathbf{x}_i^{dbc}\}_{i=1}^{N_{dbc}}$, where N_{col} , N_{freebc} , N_{nbcj} and N_{dbc} denote the number of points, respectively. Generally, the PINN loss function in our paper is of the form:

$$\begin{aligned} \mathcal{L}(\Theta) &= \mathcal{L}(\theta, \alpha_0, \alpha_1, \alpha_2, \alpha_3, \alpha_4, P_1, \dots, P_{N_{load}}) = \sum_{i=0}^4 \left(\frac{1}{2\alpha_i^2} \mathcal{L}_i + \log(1 + \alpha_i^2) \right), \\ \mathcal{L}_0 &= MSE_{dbc} = \frac{1}{N_{dbc}} \sum_{i=1}^{N_{dbc}} \left\| \bar{\mathbf{u}}(\mathbf{x}_i^{dbc}; \Theta) - \bar{\mathbf{u}}^*(\mathbf{x}_i^{dbc}) \right\|_2^2, \\ \mathcal{L}_1 &= MSE_{pde} = \frac{1}{N_{col}} \sum_{i=1}^{N_{col}} \left\| \bar{\nabla}_{\bar{\mathbf{x}}} \cdot \bar{\sigma}(\mathbf{x}_i^{col}; \Theta) \right\|_2^2, \\ \mathcal{L}_2 &= MSE_{freebc} = \frac{1}{N_{freebc}} \sum_{i=1}^{N_{freebc}} \left\| \bar{\sigma}(\mathbf{x}_i^{freebc}; \Theta) \cdot \mathbf{n}(\mathbf{x}_i^{freebc}) \right\|_2^2, \\ \mathcal{L}_3 &= \sum_{j=1}^{N_{load}} MSE_{nbcj} = \sum_{j=1}^{N_{load}} \frac{1}{N_{nbcj}} \sum_{i=1}^{N_{nbcj}} \left\| \bar{\sigma}(\mathbf{x}_i^{nbcj}; \Theta) \cdot \mathbf{n}(\mathbf{x}_i^{nbcj}) - P_j \right\|_2^2, \\ \mathcal{L}_4 &= MSE_{data} = \frac{1}{N_{col}} \sum_{i=1}^{N_{col}} \left\| \bar{\mathbf{u}}(\mathbf{x}_i^{col}; \Theta) - \bar{\mathbf{u}}^*(\mathbf{x}_i^{col}) \right\|_2^2, \end{aligned} \quad (20)$$

here, α_i is the noise parameter for each task and \mathbf{n} is the unit normal vector to the boundary surface. The non-dimensionalized stress tensor $\bar{\sigma}$ is obtained from the second order derivative of the outputs $\bar{\mathbf{u}}$ w.r.t the inputs $\bar{\mathbf{x}}$.

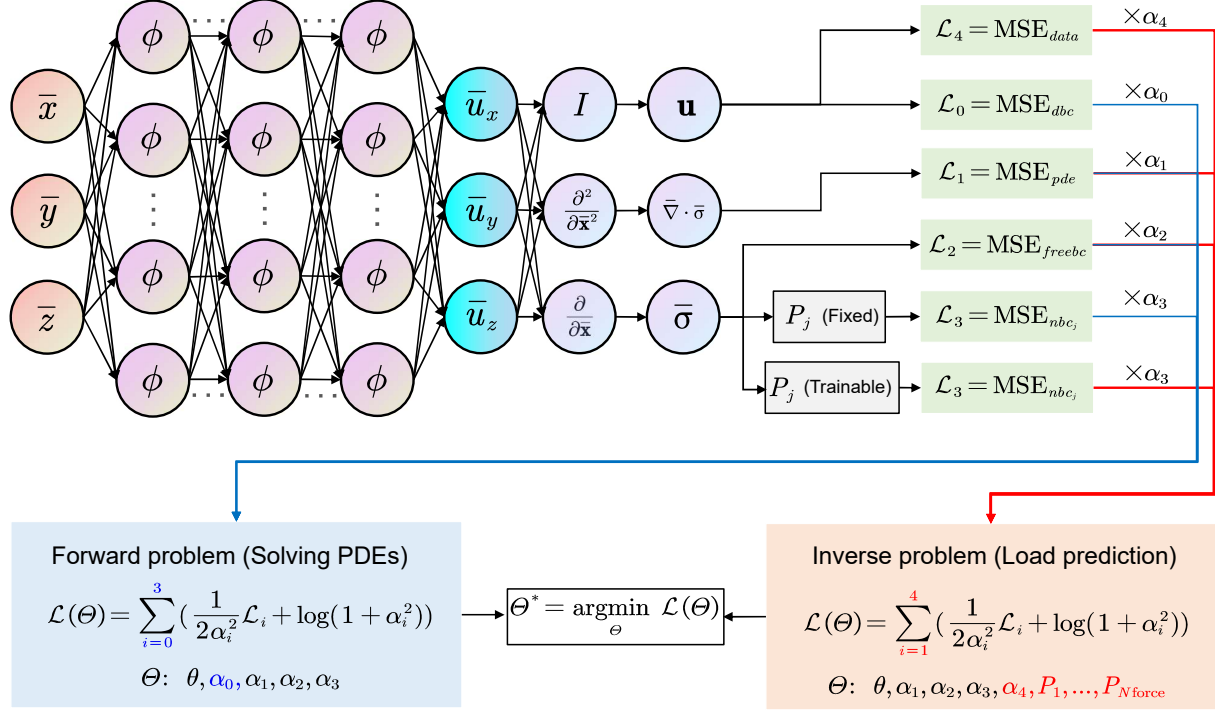


Figure 2: A demonstration of the setup of the proposed PINN method (with different learnable parameters marked in blue and red respectively)

As shown in Fig. 2, the PINN model can be trained for two different purposes by customizing the loss function $\mathcal{L}(\Theta)$ with the set of various loss tasks:

- *Forward problems:* Specifically for solving linear elastic problems using PINNs, architectures can be modified to satisfy exactly the governing PDEs (\mathcal{L}_1), free boundary conditions (\mathcal{L}_2), Neumann boundary conditions (\mathcal{L}_3), and Dirichlet boundary conditions (\mathcal{L}_0). The training parameters Θ are hereby comprised of network parameters θ and task weights $\{\alpha_0, \alpha_1, \alpha_2, \alpha_3\}$.
- *Inverse problems:* When an inverse analysis (e.g. load prediction in this paper) is required, the supervised loss term \mathcal{L}_4 can be further incorporated into $\mathcal{L}(\Theta)$. \mathbf{u}^* are observational data measurements of displacement \mathbf{u} which can be collected from either in-situ tests or from laboratory experiments. Note that the loss \mathcal{L}_0 is discarded in our inverse problems, because the observational data can automatically help fulfill the prescription of Dirichlet boundary conditions. In addition to the general trainable parameters $\{\theta, \alpha_1, \alpha_2, \alpha_3, \alpha_4\}$ which are similar to that in forward problems, the unknown physical quantities $\{P_j\}_{j=1}^{N_{load}}$ are also involved, where N_{load} denote the number of loads. (leaf node in computational graph)

Engineering structures are mostly composed of geometrically similar solid instances, for example, tunnels are assembled with identical segmented lining rings. This enlightened us to adopt transfer learning [75], which is a very popular approach in the field of natural language processing and computer vision. Several previous studies combining PINN and transfer learning have been carried out for solving forward problems, e.g. brittle fracture simulations [76] and multi-fidelity analyses [77]. Conventional machine learning is designed to work in isolation for specific tasks. Models have to be rebuilt from ground up once the scenario changes. In transfer learning, knowledge from previously trained models can be leveraged for new tasks, which can significantly accelerate the training process. In an actual tunneling project, it is often required to evaluate the structural behavior of the tunnel lining at multiple tunnel cross-sections. This process can be facilitated if external acting loads around the tunnel can be quantified appropriately for a simple scenario. Information from the simple scenario can then be used for the prediction of complicated loading scenarios at various cross-sections. This is where transfer learning has come into play. As depicted in Fig. 3 (a), in the transfer learning process, weights and biases of the initial three layers from the previously trained neural network will be frozen/fixed, while the remaining parameters will be fine-tuned with a smaller learning rate. The advantage of the approach is two-folds. First, frozen parameters ensure that the extracted features are retained, which means that the geometric similarity of the tunnel cross-section can be exploited. Second, the saved parameters are likely to be very close to the optimal parameters for the new task (shown in Fig. 3 (b)). As a result, the total number of parameters to be updated is greatly reduced and the training epochs required to get convergence is much smaller. The overall framework of the proposed PINN for the inverse analysis of tunnel structures is presented in Algorithm 1.

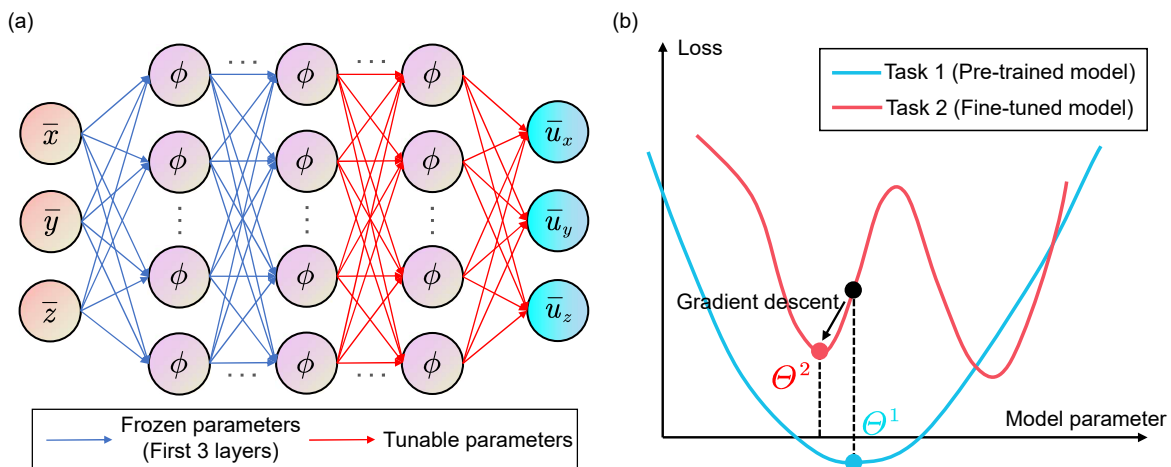


Figure 3: A schematic of transfer learning: (a) Update of network parameters and (b) Loss function convergence over iteration steps

Algorithm 1 Transfer learning based boundary-condition-learnable PINNs for the inverse analysis of loading conditions on tunnel lining rings

- 1: Determine a simplified tunneling scenario (geometry, material property, and external loads, etc.) at the offline stage.
 - 2: Build a finite element model and run the simulation to obtain displacement results $\mathbf{u}^*(\mathbf{x}_i^{col})$ at all nodes of a tunnel ring.
 - 3: Generate the coordinates of sampling points $\{\mathbf{x}_i^{col}\}_{i=1}^{N_{col}}$, $\{\mathbf{x}_i^{freebc}\}_{i=1}^{N_{freebc}}$, $\{\mathbf{x}_i^{nbcj}\}_{i=1}^{N_{nbcj}}$.
 - 4: Initialize the neural network $NN(\mathbf{x}; \theta)$, task weights α_i and unknown loads P_j .
 - 5: Minimize the loss function to compute the optimal parameter Θ_0^* . ▷ Eq. (20)
 - 6: Save the neural network parameters θ_0^* (weights and biases).
 - 7: **for** $n = 1, \dots, N$ **do**
 - 8: Select the tunnel cross-section S_n to be analyzed at the online stage.
 - 9: Obtain the displacement measurements at some selected monitoring points of S_n .
 - 10: Generate the coordinates of sampling points $\{\mathbf{x}_i^{col}\}_{i=1}^{N_{col}}$, $\{\mathbf{x}_i^{freebc}\}_{i=1}^{N_{freebc}}$, $\{\mathbf{x}_i^{nbcj}\}_{i=1}^{N_{nbcj}}$.
 - 11: Obtain the displacements $\mathbf{u}^*(\mathbf{x}_i^{col})$ at all points \mathbf{x}_i^{col} using Kriging method.
 - 12: Load the neural network parameters θ_0^* as a pre-trained model.
 - 13: Freeze the initial three layers and fine-tune the remaining network parameters.
 - 14: Initialize task weights α_i and unknown loads P_j .
 - 15: Minimize the loss function to compute the optimal parameter Θ_n^* . ▷ Eq. (20)
 - 16: **Results: predicted external loads P_j acting on the tunnel lining.**
 - 17: **end for**
-

The machine learning processes were implemented in Pytorch [68], and all the parameters were optimized using the Adam optimizer [78]. Details on the hyper-parameter settings are shown in Table 1. The neural networks were trained in Google Colab on a NVIDIA Tesla P100 GPU.

Table 1: Hyperparameters setting in the codes

	Initial value	learning rate
Neural network parameter θ	Default weight initialization	0.001
Task weights α_i	1.0	0.0001
Unknown loads P_j	1.0	0.001
Tunable parameters in transfer learning	-	0.0005

3. Numerical experiments

In the following, we present five numerical examples that illustrate the performance of the proposed PINN method in the context of a forward problem (Section 3.1) and four inverse problems (Section 3.2). In order to demonstrate the performance of the proposed method in both 2D and 3D inverse analyses, the example in Section 3.2.1 is concerned with a 3D problem, while the remaining examples (in Section 3.2.2, Section 3.2.3, and

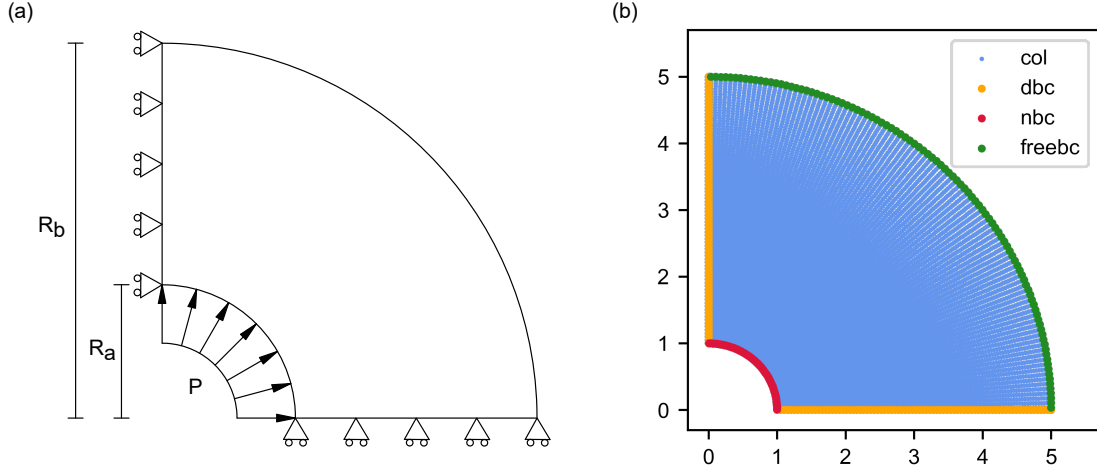


Figure 4: A schematic of transfer learning: (a) update of network parameters and (b) loss function convergence over iteration steps

Section 3.2.4) are associated with 2D tunnel rings. Furthermore, the efficiency of transfer learning concept for the training of NNs in an inverse analysis is also illustrated in Section 3.2.3 and Section 3.2.4.

3.1. Forward benchmark problem: Thick cylinder under internal pressure

The first example is a classical benchmark problem of a thick elastic cylinder which is subjected to internal pressure. The analysis is formulated as a two dimensional plane stress problem. Three different methods, i.e. plain PINN, dimensionless PINN and dimensionless PINN with multi-task learning, are implemented for comparison. The dimensionless PINN here means that no weight is assigned to each learning task, while the plain PINN is more simplified, where all the physical quantities maintain unscaled. Figure 4 (a) illustrates the geometry and the boundary conditions for this problem. The neural networks are trained using a grid of 80×80 training points, i.e. $N_{col} = 6400$, over the computational domain (see Fig. 4 (b)). The boundary conditions are trained with an additional 80 training points per edge, i.e. $N_{nbc} = N_{freebc} = 80$; $N_{dbc} = 160$.

As a reference, the analytical solution for the displacement field in x and y -axis is

$$\begin{aligned}
 u_x &= \frac{R_a^2 P r}{E (R_b^2 - R_a^2)} \left(1 - \nu + \left(\frac{R_b}{r} \right)^2 (1 + \nu) \right) \cos \theta, \\
 u_y &= \frac{R_a^2 P r}{E (R_b^2 - R_a^2)} \left(1 - \nu + \left(\frac{R_b}{r} \right)^2 (1 + \nu) \right) \sin \theta,
 \end{aligned} \tag{21}$$

and the components of the stress field obtained are provided below:

$$\begin{aligned}\sigma_{rr}(r, \beta) &= \frac{R_a^2 P}{R_b^2 - R_a^2} \left(1 - \frac{R_b^2}{r^2}\right), \\ \sigma_{\beta\beta}(r, \beta) &= \frac{R_a^2 P}{R_b^2 - R_a^2} \left(1 + \frac{R_b^2}{r^2}\right), \\ \sigma_{r\beta}(r, \beta) &= 0,\end{aligned}\tag{22}$$

where $\{r, \beta\}$ denote polar coordinates with origin in the center. The inner radius and outer radius of the cylinder are $R_a = 1$ and $R_b = 5$ respectively. The pressure P is applied on the inner circular edge with $P = 20$. The material properties considered for this example are $E = 1 \times 10^5$ and $\nu = 0.3$. The scaling factors for non-dimensionalization are chosen as $l_c = 5.0$ and $u_c = 0.0003$. The Dirichlet boundary conditions are a-priori fulfilled by defining:

$$\hat{u}_x = \bar{u}_x \times \bar{y}, \quad \hat{u}_y = \bar{u}_y \times \bar{x}.\tag{23}$$

In Fig. 5 we compare the prediction results after 50000 training steps. Compared to that of plain PINN, the maximum L_2 error of field outputs after non-dimensionalization is reduced from over 100% to less than 3%, which indicates that the non-dimensionalization can significantly improve the performance of PINN. Removing the units of measurement enables not only the comparability of each term in the loss function but also the feature normalization of both network input and output. Considering the relative L_2 error (shown in Fig. 5) of results, multi-task learning can further increase the accuracy by ensuring that each task in the loss function is learned simultaneously during gradient descent. Figure 6 shows the convergence of each individual term in the loss function.

3.2. Inverse problem: Prediction of external loads on structures

The observational data involved in this section are technically supposed to be obtained from actual experiments/measurements. In this paper, synthetic data obtained from finite element simulations are considered as measured data in order to evaluate the prediction capability of PINN models. The nodes of finite element model and their displacements are regarded as collocation training points and ground truth data for supervised learning, respectively.

3.2.1. 3D beam under uniaxial tension

The first example considers a $10 \times 2 \times 2$ beam as shown in Fig. 7 (a). A tensile load $P = 2.0$ is applied uniformly at both ends of the beam. The material properties of the beam are $E = 500$ and $\nu = 0.3$. The scaling factors are chosen as $l_c = 5.0$ and $u_c = 0.04$. The FEM solution is generated from a $100 \times 20 \times 20$ elements uniform mesh. The boundary conditions points are selected uniformly with the spacing of 0.005. To evaluate the effect of noise in the observational data on the performance of PINN, we add white Gaussian noise to the exact FEM solution \mathbf{u}^{**} to obtain the displacement fields \mathbf{u}^* . The L_2 norm errors between \mathbf{u}^* and \mathbf{u}^{**} are 10.690%, 9.292%, and 9.914% in X, Y and Z directions, respectively.

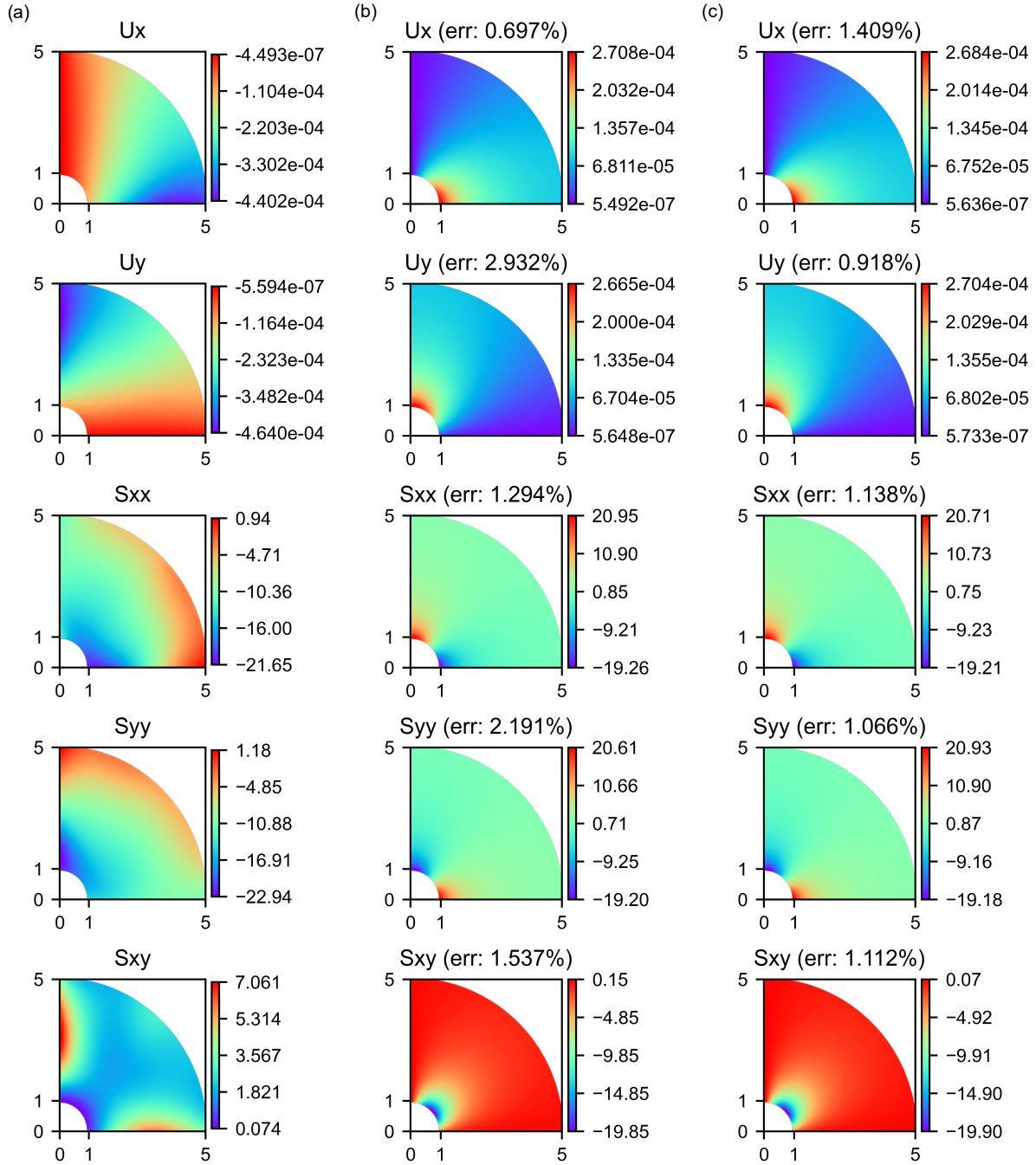


Figure 5: Displacement and stress components of thick cylinder under internal pressure: (a) plain PINN, (b) dimensionless PINN and (c) dimensionless PINN with multi-task learning

Figure 7 (b) shows the convergence of the unknown tensile load after 20,000 training epochs, with the final trained load $P = 2.00207$ (error: 0.207%), which demonstrates adequate accuracy. In addition, we also track the mean square error between PINN predictions

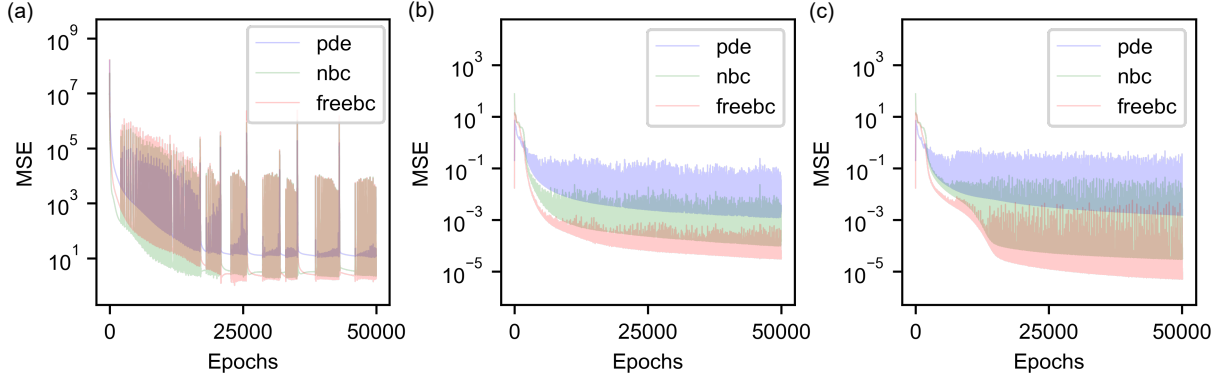


Figure 6: Evolution of all loss terms for the benchmark problem: (a) plain PINN, (b) dimensionless PINN and (c) dimensionless PINN with multi-task learning

and the ground truth FEM solution \mathbf{u}^{**} , which reads as:

$$MSE_{true} = \frac{1}{N_{col}} \sum_{i=1}^{N_{col}} \|\bar{\mathbf{u}}(\mathbf{x}_i^{col}; \Theta) - \bar{\mathbf{u}}^{**}(\mathbf{x}_i^{col})\|_2^2. \quad (24)$$

Figures 7 (c) and 7 (d) show evolution of all loss terms associated with Eq. (20) and Eq. (24). It is noteworthy that MSE_{data} , see Eq. 20, is always fluctuating but not decreasing further after 5000 training epochs, denoting that the involvement of physics laws prevent the neural network from overfitting on noisy data. However, MSE_{true} keeps dropping even to the magnitude of 10^{-7} , which indicates that PINN method can identify the correct solution from noisy data (even those with an error of around 10%) and is robust to Gaussian noise.

3.2.2. 2D tunnel ring with two acting loads (2p): training from the beginning

From section 3.2.2 we focus on the inverse analysis of the tunnel lining, which is considered as a two-dimensional homogeneous isotropic ring. Given that the dimension of tunnel length is very large compared to the others, the problem can be regarded as a plane strain problem. In this part, the steps 1-6 at the offline stage in Algorithm 1 are carried out.

As shown in Fig. 8 (a), the tunnel ring has an outer radius of $4m$ and a thickness of $0.5m$. In light of the surrounding pressure generated by the soil medium, two uniformly distributed pressures $P_1 = 100kN$ and $P_2 = 80kN$ are directly applied on the structure, which can be considered as simplified vertical and lateral soil pressures respectively. Thus the research subject in section 3.2.2 is referred to as case 2p. The modulus of elasticity of concrete is $30GPa$, and the Poisson's ratio is 0.2. The scaling parameters are chosen as $l_c = 4.0$ and $u_c = 0.0018$.

Figure 8 (b) depicts the sampling scheme of uniformly distributed training points for case 2p. Considering the sensor noise and environmental disturbance in the practical tunnel monitoring, some Gaussian noise are added to the exact FEM solution \mathbf{u}^{**} to obtain the displacement fields \mathbf{u}^* with L_2 errors of 11.250% and 10.060% in X and Y directions,

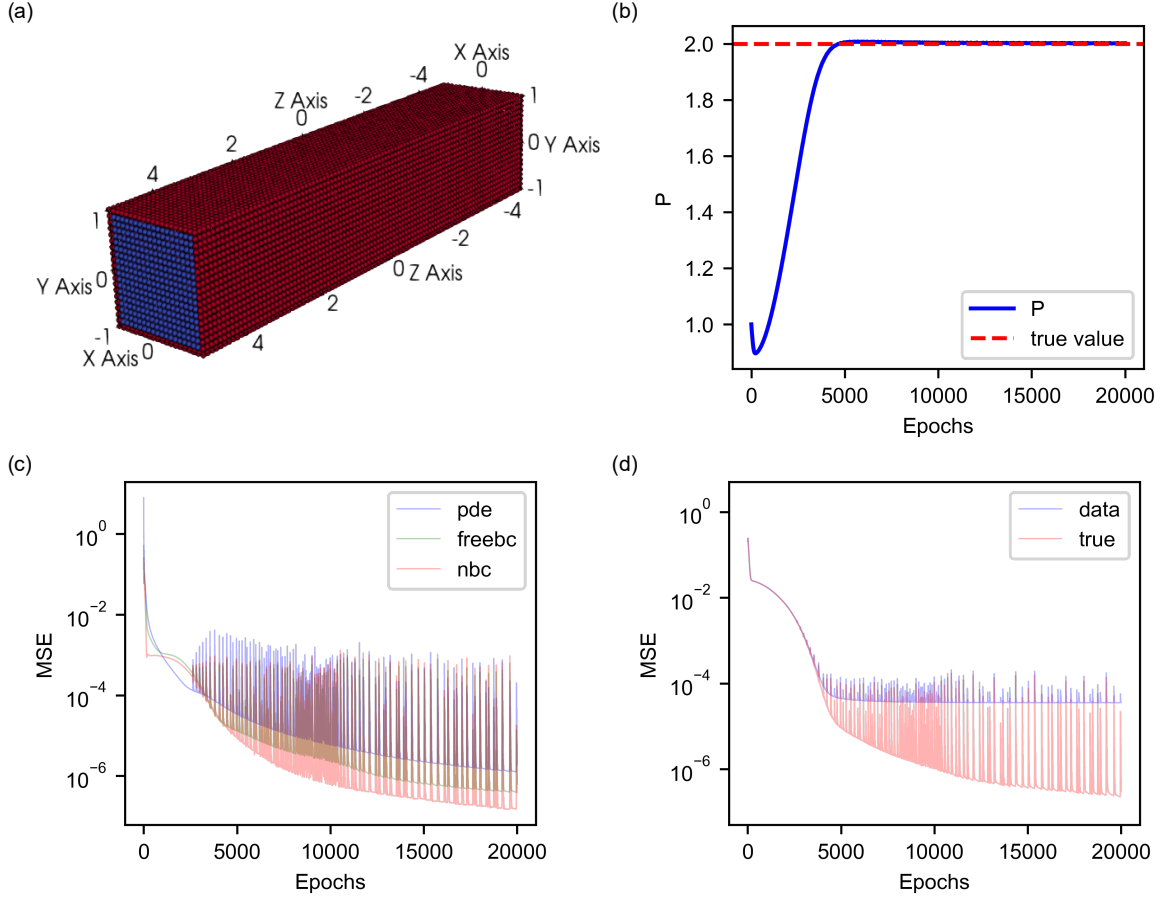


Figure 7: PINN model for prediction of 3D beam under uniaxial tension: (a) training point distribution, (b) prediction convergence of load, (c) convergence of physics loss and (d) convergence of data loss

respectively. The purpose of this procedure is also to facilitate comparison of the impact of error types on PINN’s performance in section 3.2.4.

Figure 9 shows the displacement field as well as the stress field obtained from PINN after 100000 training epochs. Figure 10 shows the convergence of the unknown load. The final solutions are $P_1 = 100.376kN$ (0.376%) and $P_2 = 81.080kN$ (1.350%), which are sufficiently accurate. The evolution of each loss term is given in Fig. 11. It can be observed that MSE_{data} hardly decreases after 25000 steps but MSE_{true} still keeps decreasing, which is similar to that of the 3D beam example.

3.2.3. 2D tunnel ring with four acting loads ($4p$): fine-tuning the pre-trained model

Here, we consider two more complicated loading conditions as shown in Fig. 12 (a) and Fig. 12 (b), where four uniformly distributed pressures are applied on the tunnel rings. Therefore, the examples in section 3.2.3 are referred to as $4p$. The structural deformation patterns are different for two loading scenarios, depending on whether the inward convergence is at the top (i.e. case $4p_a$) or from the sides (i.e. case $4p_b$). The geometry of

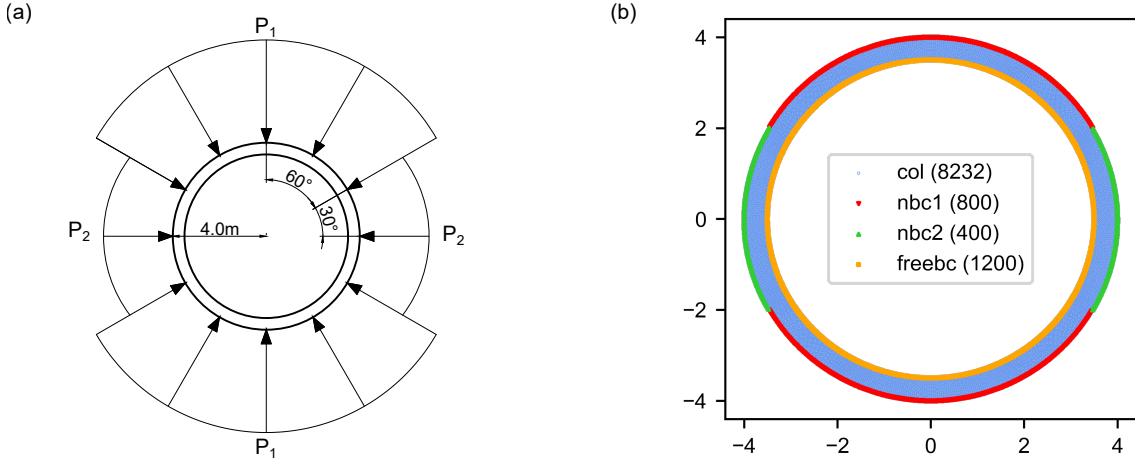


Figure 8: PINN model for prediction of loads applied on the 2D tunnel ring $2p$: (a) tunnel lining subjected to simplified vertical and lateral soil pressures ($P_1 = 100kN$ and $P_2 = 80kN$) and (b) sampling scheme of training points (Numbers of points are indicated in parentheses.)

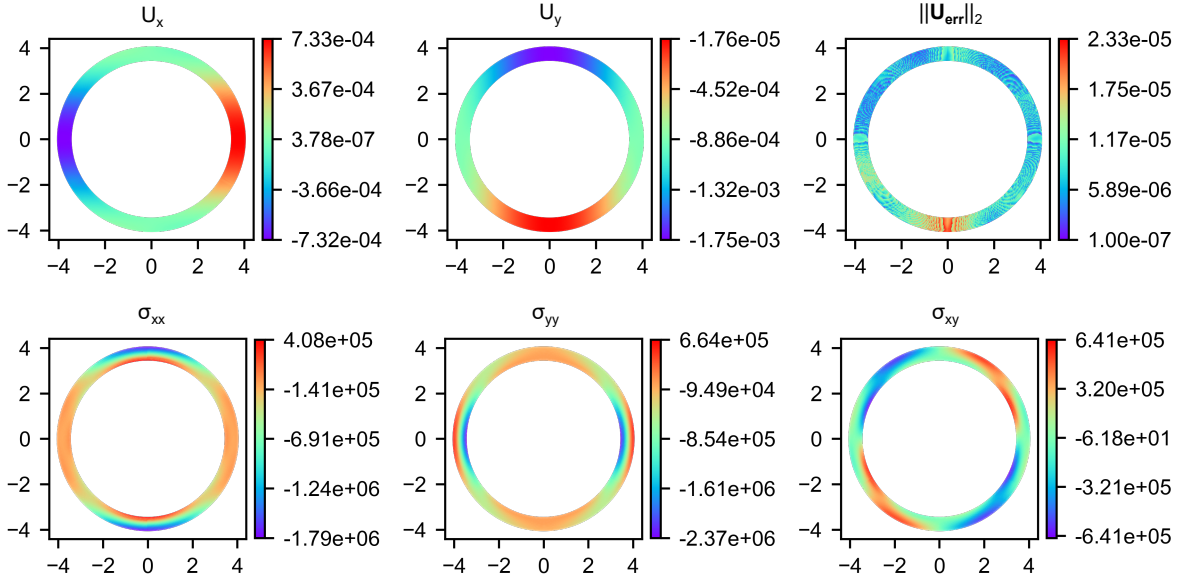


Figure 9: Resulting components of displacement vector field and stress tensor fields for case $2p$

the structure and the material properties remain the same as that in section 3.2.2. The displacement field scaling parameters are $u_c = 0.0024$ and $u_c = 0.002$, respectively.

Figure 12 (c) depicts the sampling scheme of the training points for both loading cases. Some Gaussian noise are added to the exact FEM solution \mathbf{u}^{**} to obtain the displacement fields \mathbf{u}^* with L_2 errors of 9.223% and 8.585% in X and Y directions for case $4p_a$, while L_2 errors in X and Y directions for case $4p_b$ are 8.731% and 8.814%, respectively.

According to the steps 7-17 at the online stage in Algorithm 1, we firstly froze the parameters in the first three layers of the neural network obtained from the case $2p$. The

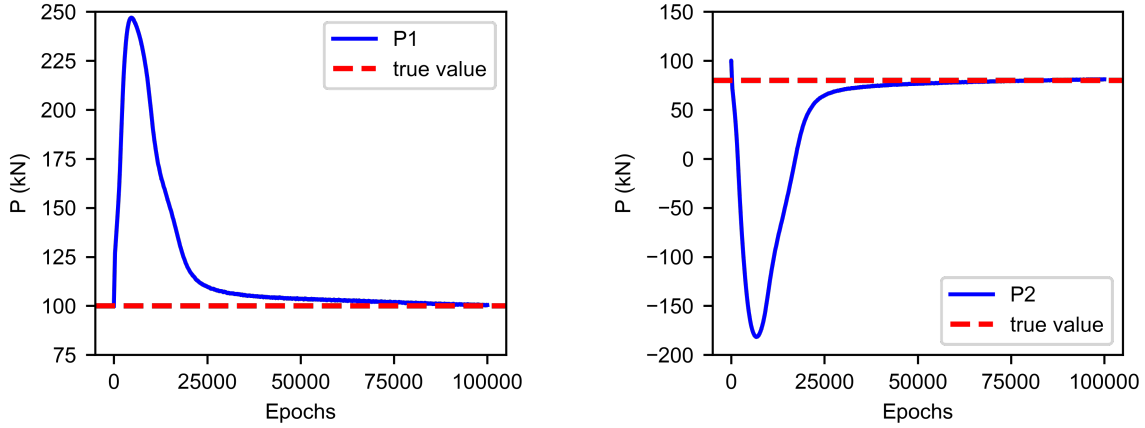


Figure 10: Convergence of external loads for case $2p$

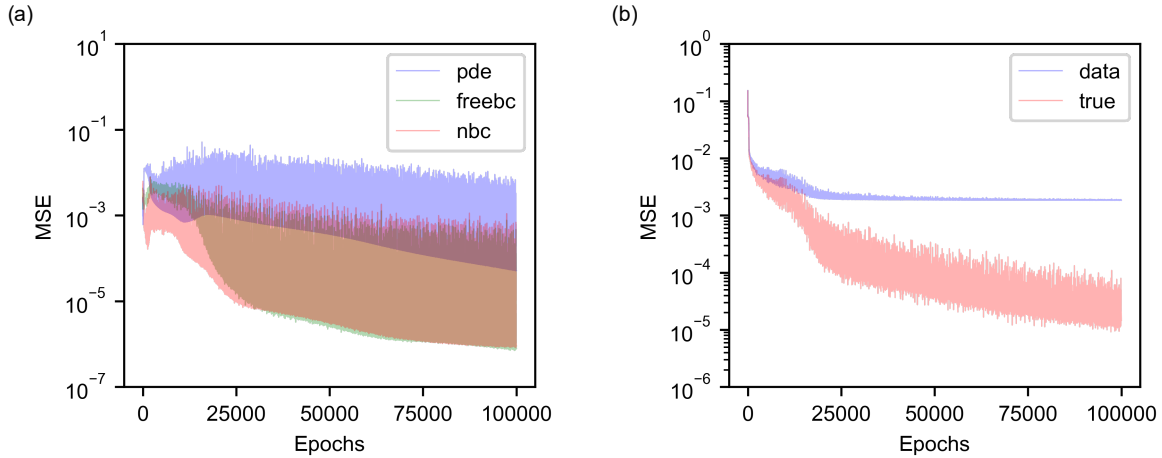


Figure 11: Convergence of loss functions: (a) physics loss and (b) data loss

remaining parameters are fine-tuned with a learning rate of 0.0005 to realize the transfer learning for $4p_a$ and $4p_b$.

Figures 13 and 14 show the convergence of the unknown loads. Tables 2 and 3 summarize all the predicted results of unknown loads for both scenarios and the corresponding computational times. In general, the inverse analysis of predicting acting loads in both cases can be solved appropriately using PINNs with transfer learning. The average prediction errors for all four acting loads in scenarios $4p_a$ and $4p_b$ are only less than 2%. Considering the pre-trained model in scenario $2p$ as the basis for transfer learning to the prediction models in both investigated cases $4p_a$ and $4p_b$, it is shown that the good prediction is achieved not only with a similar scenario to pre-trained scenario (scenarios $4p_a$ and $2p$) but also with an unlike scenario (scenarios $4p_b$ and $2p$), which shows the robustness of the proposed PINNs approach. For better comparison, we also provide the results obtained by training the neural networks without transfer learning. It can be seen that the

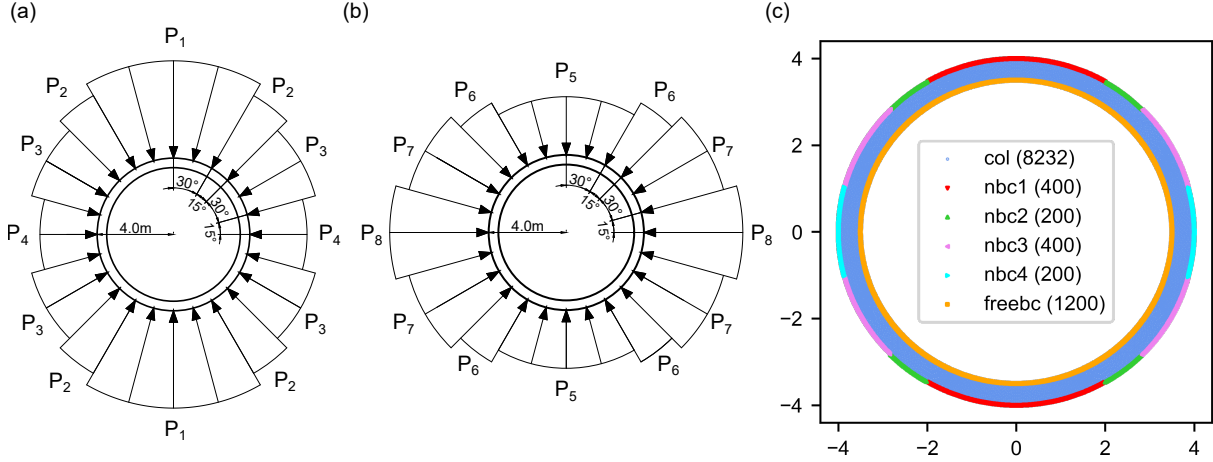


Figure 12: PINN model for prediction of loads applied on the 2D tunnel ring $4p$: (a) tunnel lining $4p_a$ subjected to four loads ($P_1 = 130kN$, $P_2 = 120kN$, $P_3 = 110kN$, $P_4 = 100kN$), (b) tunnel lining $4p_b$ subjected to another four loads ($P_5 = 100kN$, $P_6 = 110kN$, $P_7 = 120kN$, $P_8 = 130kN$) and (c) sampling scheme of training points (Numbers of points are indicated in parentheses.)

Table 2: Final predictions of PINN of case $4p_a$

	P_1	P_2	P_3	P_4	Time (min)
True value	130000	120000	110000	100000	-
Gaussian noise (transfer)	129459.8 (0.416%)	126371.8 (5.310%)	111674.5 (1.522%)	99898.7 (0.101%)	15
Gaussian noise (no transfer)	129213.4 (0.605%)	120106.6 (0.089%)	110350.7 (0.319%)	105558.6 (5.559%)	80

prediction results of transfer learning and training from the beginning are approximately close in accuracy for both cases. As shown in Fig. 3 (b), the initial network parameter for a pre-trained model does not guarantee the absolute convergence to the global optimum after gradient descent, and it may easily fall into an adjacent local minimum. The PINNs without transfer learning can also converge to a physics-obeying local minimum instead of the global minimum [79, 80]. Therefore, the final accuracy of PINN predictions based on Gaussian noisy data strongly depends on the characteristics of loss landscape. Model transfer is also robust to Gaussian noise. The parameter freezing greatly reduces the training cost and retains some physical characteristics, which speeds up the training process.

3.2.4. 2D tunnel ring with four acting loads ($4p'$): model transfer with data from Kriging

In this section, we still focus on the same loading scenarios shown in Fig. 12. For distinction, the examples in section 3.2.4 are referred to as $4p'$. For a practical-oriented application in tunnel engineering, available monitoring data are assumed to be collected from a limited number of locations around the lining ring, so Kriging interpolation has to be adopted for the reconstruction of the whole displacement field. Here we consider

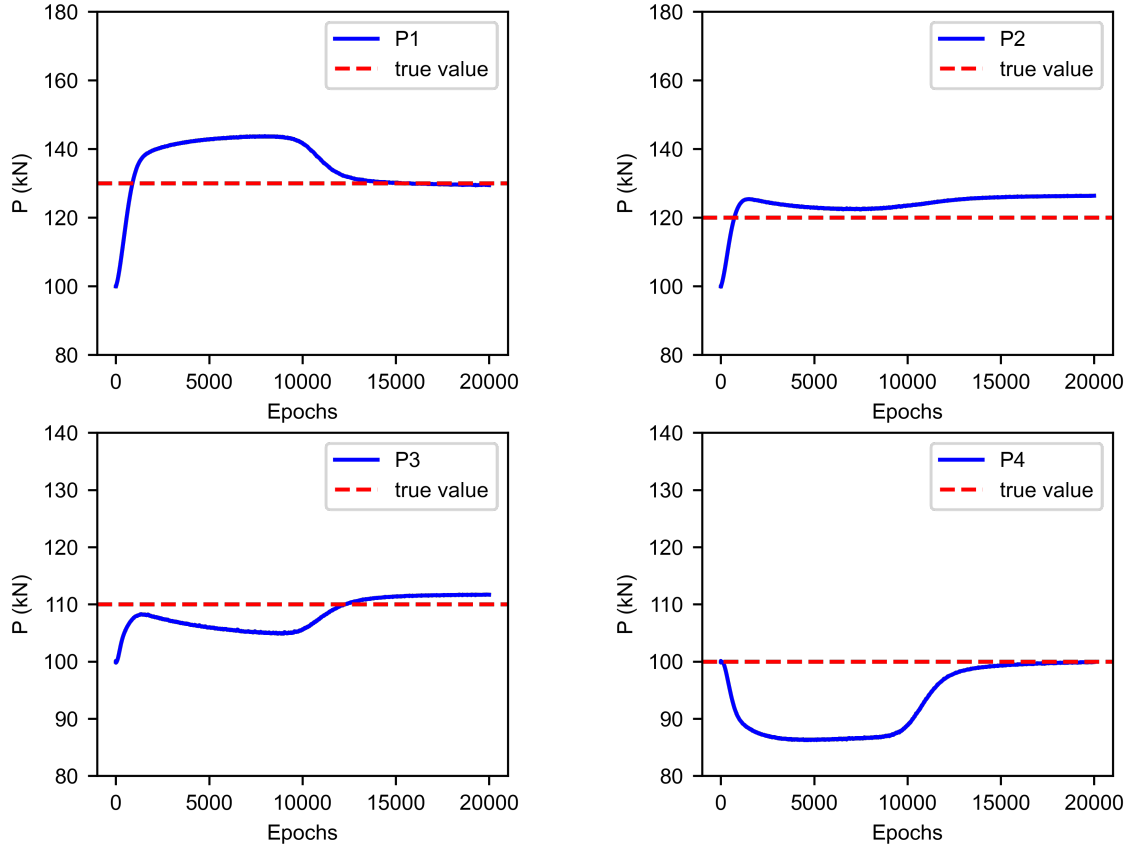


Figure 13: Convergence of external loads for case $4p.a$ based on data with Gaussian noise

Table 3: Final predictions of PINN of case $4p.b$

	P_5	P_6	P_7	P_8	Time (min)
True value	100000	110000	120000	130000	-
Gaussian noise (transfer)	100733.3 (0.733%)	108099.4 (1.728%)	119787.0 (0.178%)	132616.7 (2.013%)	15
Gaussian noise (no transfer)	101399.6 (1.400%)	111262.3 (1.148%)	122610.7 (2.176%)	123477.0 (5.018%)	80

two different monitoring schemes. For the first one, there are a total of 14 selected edges along the ring direction, with each containing 14 monitoring points. This strategy is called 14×14 and is shown in Fig. 15 (a). In addition to the 14×14 scheme, we provide another scheme 14×10 , as shown in Fig. 15 (b). The number of monitoring edges in this scheme is reduced to 10, but each edge still has 14 interpolation points. Table 4 shows all the L_2 errors of final obtained displacements \mathbf{u}^* from the Kriging method, as compared to "true" displacements from FEM simulations. Procedures at the online stage are carried out again for load prediction.

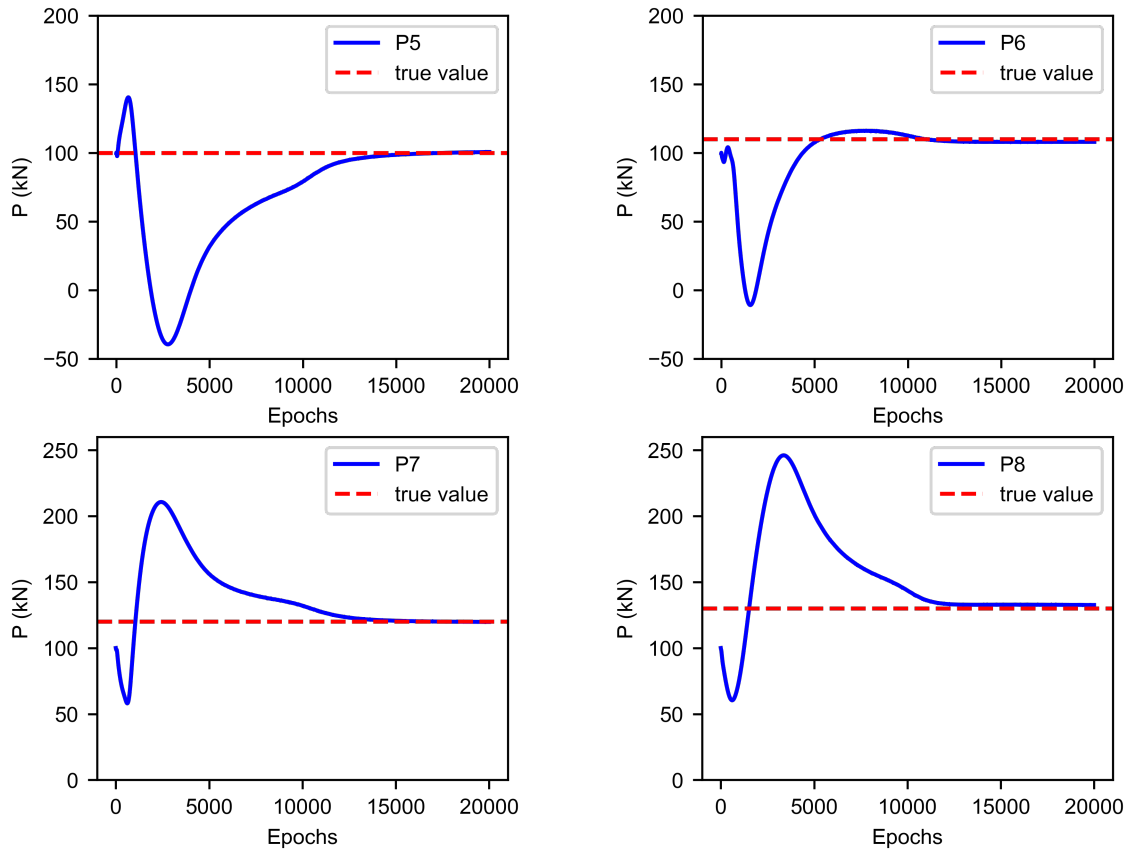


Figure 14: Convergence of external loads for case $4p.b$ based on data with Gaussian noise

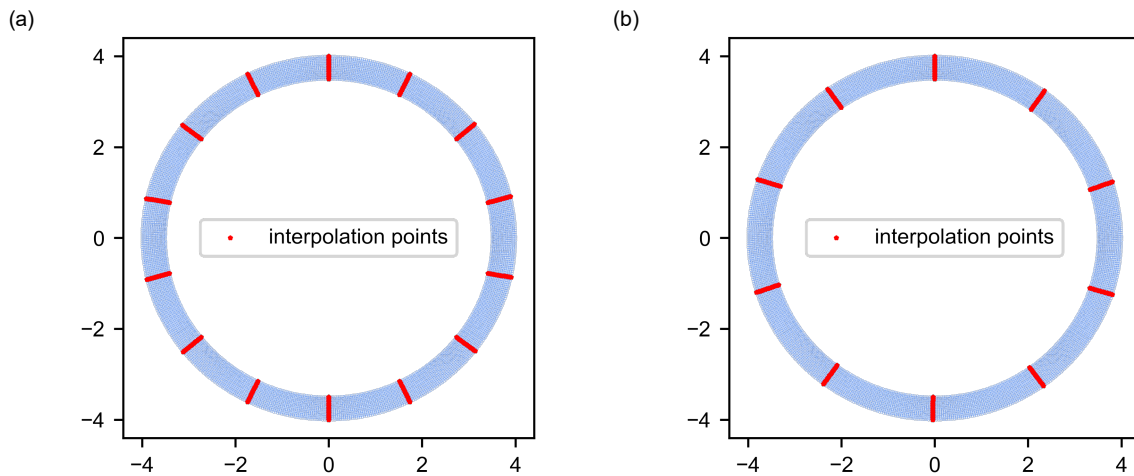


Figure 15: PINN model for prediction of loads applied on the 2D tunnel ring $4p$: (a) tunnel lining subjected to a more complicated loading condition, (b) sampling scheme of training points (Numbers of points are indicated in parentheses.), (c) Kriging scheme 14×14 and (d) Kriging scheme 14×10

Table 4: L_2 error of Kriging interpolation

	L_2 error in X-direction	L_2 error in Y-direction
$4p'_a$ (14×14)	5.742%	2.066%
$4p'_a$ (14×10)	20.660%	7.991%
$4p'_b$ (14×14)	4.236%	1.833%
$4p'_b$ (14×10)	21.180%	11.500%

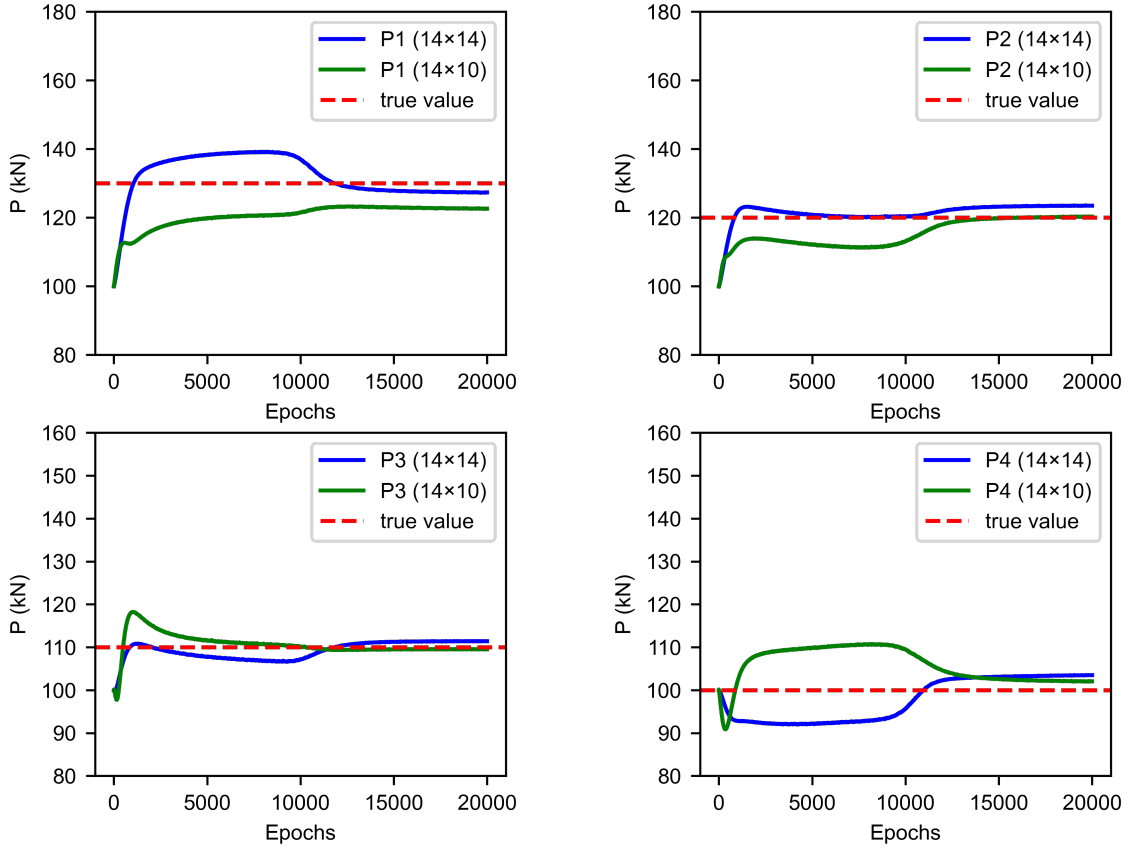


Figure 16: Convergence of external loads for case $4p'_a$ based on data from Kriging

Figures 16 and 17 show the convergence of the unknown loads for cases $4p'_a$ and $4p'_b$, respectively. Tables 5 and 6 summarize all the predicted results of unknown loads for all schemes and the corresponding computational times. For better comparison, we also provide the results obtained by training the neural networks without transfer learning. In general, the prediction results using transfer learning are more accurate than those trained from the beginning for both Kriging reconstruction schemes in two loading scenarios. The predictions accuracy is still within the acceptable tolerance even when the Kriging interpolation error reaches 20% in the 14×10 scheme. Prior knowledge inherited from the pre-trained model can greatly avoid the over-fitting on data with large errors. With regard

Table 5: Final predictions of PINN of case $4p'_a$

	P_1	P_2	P_3	P_4	Time (min)
True value	130000	120000	110000	100000	-
14×14 (transfer)	127335.8 (2.049%)	123462.2 (2.885%)	111400.0 (1.273%)	103479.2 (3.479%)	15
14×14 (no transfer)	127251.3 (2.114%)	119330.1 (0.558%)	109521.9 (0.435%)	110568.9 (10.569%)	80
14×10 (transfer)	122604.0 (5.689%)	120272.0 (0.227%)	109516.1 (0.440%)	102036.4 (2.036%)	15
14×10 (no transfer)	123200.9 (5.230%)	113619.1 (5.317%)	105053.9 (4.496%)	111488.0 (11.488%)	80

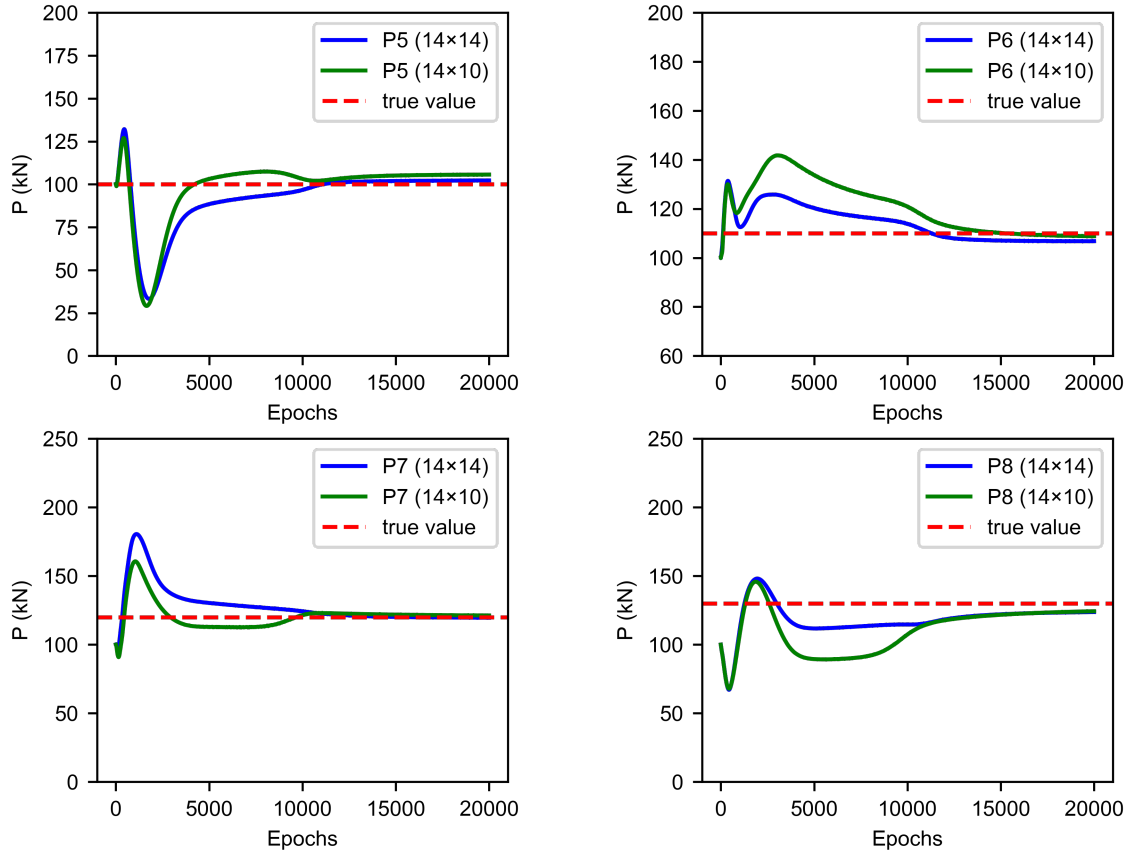


Figure 17: Convergence of external loads for case $4p'_b$ based on data from Kriging

to the computing effort, the required training time in case of adopting transfer learning is only around 15 minutes, which is suitable for real-time applications in practical tunnel projects. It is noted that although the interpolation error from Kriging method of the 14×14 scheme in case of not applying transfer learning is not that big (around 5%), the

Table 6: Final predictions of PINN of case $4p'_b$

	P_5	P_6	P_7	P_8	Time (min)
True value	100000	110000	120000	130000	-
14×14 (transfer)	102232.2 (2.232%)	106797.8 (2.911%)	119574.4 (0.355%)	123723.0 (3.103%)	15
14×14 (no transfer)	98253.0 (1.747%)	105128.4 (4.429%)	114092.1 (4.923%)	112957.0 (13.110%)	80
14×10 (transfer)	105654.5 (5.655%)	108819.7 (1.073%)	121212.5 (1.011%)	124293.3 (4.390%)	15
14×10 (no transfer)	88882.5 (11.118%)	94828.8 (13.792%)	105704.6 (11.913%)	100056.6 (23.033%)	80

prediction for load P_4 (exceeding the tolerance of 10%) is not as good as compared to the predictions for loads P_1, P_2 and P_3 (less than 3%). While, the prediction errors for all loads are more evenly distributed around 1% to 3% if transfer learning is adopted. In this example, using transfer learning can outperform the traditional approach, which is the training NNs from scratch. In addition, the inaccurate prediction indicates also the sensitivity of PINNs to the noise type. Follow-up work should be shifted to some other generative models for field reconstructions, which will be discussed in detail in the next section.

4. Conclusions

In this paper, the following conclusions can be drawn: (1) The non-dimensionalization of the governing equation of elasticity and the utilization of homoscedastic uncertainty in Bayesian modeling to capture the relative confidence between different learning tasks have significantly improved the performance of PINNs; (2) In case of setting the labels of boundary conditions as learnable parameters, with the support of enough observational data (even those with noise) and under the regularization of physics laws, the neural network is successfully characterized the unknown loads of a structural system; (3) The introduced transfer learning based two-stage learning approach has been successfully applied to the inverse analysis of tunnel structures, i.e. predicting the undiscovered surrounding pressures based on a limited number of displacement measurements. Although the offline model is trained previously in a simplified scenario, some physics features can be extracted and exploited, which guides the neural network at the online stage to accurately predict external loads. Good predictions for unknown acting loads are obtained not only in a scenario with similar boundary conditions but also with unlike conditions as compared to the boundary conditions in the pre-trained scenario. Furthermore, the computational cost is significantly reduced, which enables for a real-time application in practice tunnel engineering.

While numerical results presented in this paper show that our approach is promising for the inverse analysis of tunnel structures, some extensions to this work can be addressed

in future studies. For the analysis of tunnel structures, we assume that the surrounding pressure is uniformly distributed on several specific regions. The effect of the number of loads on the prediction accuracy still needs further investigation. Concentrated loads should also be taken into consideration. Moreover, the tunnel lining can be modeled as segmental lining for a more realistic representation. The joints between lining segments must be considered to account for the displacement components arising from kinematics. Although Kriging is an effective interpolation method, the generated interpolation error, even that of small values, may lead to the neural network's convergence to incorrect solutions. Since neural networks are very robust to Gaussian noise, some other generative models can be utilized instead of Kriging models for the reconstructions of displacement fields, e.g. generative adversarial networks (GANs) and variational autoencoders (VAEs). The displacement fields reconstructed by such models usually have Gaussian noise, which can be well handled by PINNs as shown in Section 3.2.3, while the layout of monitoring points can be more flexible. In this paper, the monitoring points are uniformly distributed, however, in practice even fewer sensors are usually installed only on the inner surface of tunnel linings. With these deep learning based inpainting approaches, displacement field reconstruction can be more easily achieved.

5. Acknowledgment

The first author acknowledges the support from the China Scholarship Council (CSC). The authors also gratefully acknowledge financial support by the National Natural Science Foundation of China under Grant 51808336 and the Key Project of High-speed Rail Joint Fund of National Natural Science Foundation of China under Grant U1934210.

References

- [1] C. Hellmich, H. Mang, and F.-J. Ulm, “Hybrid method for quantification of stress states in shotcrete tunnel shells: combination of 3d in situ displacement measurements and thermochemoplastic material law,” *Computers & Structures*, vol. 79, no. 22-25, pp. 2103–2115, 2001.
- [2] R. Lackner, J. Macht, and H. Mang, “Hybrid analysis method for on-line quantification of stress states in tunnel shells,” *Mechanics and Engineering*, vol. 195, no. 41-43, pp. 5361–5376, 2006.
- [3] B. Pichler and C. Hellmich, “Hybrid methods for shotcrete and segmental linings tunnel shells – combining displacement and rotation measurements with computational multiscale mechanics,” *Geomechanics and Tunnelling*, vol. 11, no. 3, pp. 226–235, 2018.
- [4] J.-L. Zhang, C. Vida, Y. Yuan, C. Hellmich, H. A. Mang, and B. Pichler, “A hybrid analysis method for displacement-monitored segmented circular tunnel rings,” *Engineering Structures*, vol. 148, pp. 839–856, 2017.
- [5] R. Fuentes, “Internal forces of underground structures from observed displacements,” *Tunnelling and Underground Space Technology*, vol. 49, pp. 50–66, 2015.
- [6] W. He, L. Xu, and L. Wang, “Theoretical back analysis of internal forces of primary support in deep tunnels,” *Journal of Engineering Science and Technology Review*, vol. 12, no. 1, pp. 18–26, 2019.
- [7] Y. Zhang, J. Karlovsek, and X. Liu, “Identification method for internal forces of segmental tunnel linings via the combination of laser scanning and hybrid structural analysis,” *Sensors*, vol. 22, no. 6, p. 2421, 2022.
- [8] Y. Lecun, Y. Bengio, and G. Hinton, “Deep learning,” *Nature*, vol. 521, pp. 436–444, may 2015.
- [9] K. Duraisamy, G. Iaccarino, and H. Xiao, “Turbulence modeling in the age of data,” *Annual Review of Fluid Mechanics*, vol. 51, pp. 357–377, 2019.
- [10] S. L. Brunton, B. R. Noack, and P. Koumoutsakos, “Machine Learning for Fluid Mechanics,” *Annual Review of Fluid Mechanics*, vol. 52, pp. 477–508, 2020.
- [11] L. Zhang, J. Han, H. Wang, R. Car, and E. Weinan, “Deep Potential Molecular Dynamics: A Scalable Model with the Accuracy of Quantum Mechanics,” *Physical Review Letters*, vol. 120, no. 14, p. 143001, 2018.
- [12] J. Han, A. Jentzen, and E. Weinan, “Solving high-dimensional partial differential equations using deep learning,” *Proceedings of the National Academy of Sciences of the United States of America*, vol. 115, no. 34, pp. 8505–8510, 2018.

- [13] D. Z. Huang, K. Xu, C. Farhat, and E. Darve, “Learning constitutive relations from indirect observations using deep neural networks,” *Journal of Computational Physics*, vol. 416, p. 109491, sep 2020.
- [14] K. Wang and W. C. Sun, “Meta-modeling game for deriving theory-consistent, microstructure-based traction–separation laws via deep reinforcement learning,” *Computer Methods in Applied Mechanics and Engineering*, vol. 346, pp. 216–241, 2019.
- [15] K. Linka, M. Hillgärtner, K. P. Abdolazizi, R. C. Aydin, M. Itskov, and C. J. Cyron, “Constitutive artificial neural networks: A fast and general approach to predictive data-driven constitutive modeling by deep learning,” *Journal of Computational Physics*, vol. 429, p. 110010, mar 2021.
- [16] Y. C. Hsu, C. H. Yu, and M. J. Buehler, “Using Deep Learning to Predict Fracture Patterns in Crystalline Solids,” *Matter*, vol. 3, no. 1, pp. 197–211, 2020.
- [17] X. Liu, C. E. Athanasiou, N. P. Padture, B. W. Sheldon, and H. Gao, “A machine learning approach to fracture mechanics problems,” *Acta Materialia*, vol. 190, pp. 105–112, 2020.
- [18] M. Mozaffar, R. Bostanabad, W. Chen, K. Ehmann, J. Cao, and M. A. Bessa, “Deep learning predicts path-dependent plasticity,” *Proceedings of the National Academy of Sciences of the United States of America*, vol. 116, no. 52, pp. 26414–26420, 2019.
- [19] X. Li, Z. Liu, S. Cui, C. Luo, C. Li, and Z. Zhuang, “Predicting the effective mechanical property of heterogeneous materials by image based modeling and deep learning,” *Computer Methods in Applied Mechanics and Engineering*, vol. 347, pp. 735–753, 2019.
- [20] L. Lu, M. Dao, P. Kumar, U. Ramamurty, G. E. Karniadakis, and S. Suresh, “Extraction of mechanical properties of materials through deep learning from instrumented indentation,” *Proceedings of the National Academy of Sciences of the United States of America*, vol. 117, no. 13, pp. 7052–7062, 2020.
- [21] B. T. Cao, S. Freitag, and G. Meschke, “A hybrid RNN-GPOD surrogate model for real-time settlement predictions in mechanised tunnelling,” *Advanced Modeling and Simulation in Engineering Sciences*, vol. 3, no. 5, pp. 1–22, 2016.
- [22] S. Freitag, B. T. Cao, J. Ninić, and G. Meschke, “Recurrent neural networks and proper orthogonal decomposition with interval data for real-time predictions of mechanised tunnelling processes,” *Computers and Structures*, vol. 207, pp. 258–273, sep 2018.
- [23] B. T. Cao, M. Obel, S. Freitag, P. Mark, and G. Meschke, “Artificial neural network surrogate modelling for real-time predictions and control of building damage during mechanised tunnelling,” *Advances in Engineering Software*, vol. 149, p. 102869, nov 2020.

- [24] A. Koeppel, F. Bamer, and B. Markert, “An intelligent nonlinear meta element for elastoplastic continua: deep learning using a new Time-distributed Residual U-Net architecture,” *Computer Methods in Applied Mechanics and Engineering*, vol. 366, p. 113088, 2020.
- [25] Z. Liu, M. A. Bessa, and W. K. Liu, “Self-consistent clustering analysis: An efficient multi-scale scheme for inelastic heterogeneous materials,” *Computer Methods in Applied Mechanics and Engineering*, vol. 306, pp. 319–341, 2016.
- [26] K. Wang and W. C. Sun, “A multiscale multi-permeability poroplasticity model linked by recursive homogenizations and deep learning,” *Computer Methods in Applied Mechanics and Engineering*, vol. 334, pp. 337–380, 2018.
- [27] M. A. Bessa, R. Bostanabad, Z. Liu, A. Hu, D. W. Apley, C. Brinson, W. Chen, and W. K. Liu, “A framework for data-driven analysis of materials under uncertainty: Countering the curse of dimensionality,” *Computer Methods in Applied Mechanics and Engineering*, vol. 320, pp. 633–667, jun 2017.
- [28] S. Saha, Z. Gan, L. Cheng, J. Gao, O. L. Kafka, X. Xie, H. Li, M. Tajdari, H. A. Kim, and W. K. Liu, “Hierarchical Deep Learning Neural Network (HiDeNN): An artificial intelligence (AI) framework for computational science and engineering,” *Computer Methods in Applied Mechanics and Engineering*, vol. 373, p. 113452, 2021.
- [29] H. J. Logarzo, G. Capuano, and J. J. Rimoli, “Smart constitutive laws: Inelastic homogenization through machine learning,” *Computer Methods in Applied Mechanics and Engineering*, vol. 373, p. 113482, 2021.
- [30] M. Raissi, P. Perdikaris, and G. E. Karniadakis, “Physics-informed neural networks: A deep learning framework for solving forward and inverse problems involving nonlinear partial differential equations,” *Journal of Computational Physics*, vol. 378, pp. 686–707, 2019.
- [31] G. E. Karniadakis, I. G. Kevrekidis, L. Lu, P. Perdikaris, S. Wang, and L. Yang, “Physics-informed machine learning,” *Nature Reviews Physics*, vol. 3, no. 6, pp. 422–440, 2021.
- [32] X. Meng, Z. Li, D. Zhang, and G. E. Karniadakis, “PPINN: Parareal physics-informed neural network for time-dependent PDEs,” *Computer Methods in Applied Mechanics and Engineering*, vol. 370, p. 113250, oct 2020.
- [33] A. D. Jagtap, E. Kharazmi, and G. E. Karniadakis, “Conservative physics-informed neural networks on discrete domains for conservation laws: Applications to forward and inverse problems,” *Computer Methods in Applied Mechanics and Engineering*, vol. 365, p. 113028, 2020.

- [34] G. Pang, M. D’Elia, M. Parks, and G. E. Karniadakis, “nPINNs: Nonlocal physics-informed neural networks for a parametrized nonlocal universal Laplacian operator. Algorithms and applications,” *Journal of Computational Physics*, vol. 422, p. 109760, 2020.
- [35] E. Kharazmi, Z. Zhang, and G. E. Karniadakis, “hp-VPINNs: Variational physics-informed neural networks with domain decomposition,” *Computer Methods in Applied Mechanics and Engineering*, vol. 374, p. 113547, 2021.
- [36] L. Yang, X. Meng, and G. E. Karniadakis, “B-PINNs: Bayesian physics-informed neural networks for forward and inverse PDE problems with noisy data,” *Journal of Computational Physics*, vol. 425, p. 109913, 2021.
- [37] H. Gao, L. Sun, and J. X. Wang, “PhyGeoNet: Physics-informed geometry-adaptive convolutional neural networks for solving parameterized steady-state PDEs on irregular domain,” *Journal of Computational Physics*, vol. 428, p. 110079, 2021.
- [38] R. Zhang, Y. Liu, and H. Sun, “Physics-informed multi-LSTM networks for meta-modeling of nonlinear structures,” *Computer Methods in Applied Mechanics and Engineering*, vol. 369, p. 113226, 2020.
- [39] L. Yang, D. Zhang, and G. E. Karniadakis, “Physics-informed generative adversarial networks for stochastic differential equations,” *SIAM Journal on Scientific Computing*, vol. 42, no. 1, pp. A292–A317, 2020.
- [40] H. Gao, M. J. Zahr, and J. X. Wang, “Physics-informed graph neural Galerkin networks: A unified framework for solving PDE-governed forward and inverse problems,” *Computer Methods in Applied Mechanics and Engineering*, vol. 390, 2022.
- [41] M. Raissi, A. Yazdani, and G. E. Karniadakis, “Hidden fluid mechanics: Learning velocity and pressure fields from flow visualizations,” *Science*, vol. 367, no. 6481, pp. 1026–1030, 2020.
- [42] Z. Mao, A. D. Jagtap, and G. E. Karniadakis, “Physics-informed neural networks for high-speed flows,” *Computer Methods in Applied Mechanics and Engineering*, vol. 360, p. 112789, 2020.
- [43] H. Wessels, C. Weißenfels, and P. Wriggers, “The neural particle method – An updated Lagrangian physics informed neural network for computational fluid dynamics,” *Computer Methods in Applied Mechanics and Engineering*, vol. 368, p. 113127, 2020.
- [44] L. Sun, H. Gao, S. Pan, and J. X. Wang, “Surrogate modeling for fluid flows based on physics-constrained deep learning without simulation data,” *Computer Methods in Applied Mechanics and Engineering*, vol. 361, p. 112732, apr 2020.

- [45] X. Jin, S. Cai, H. Li, and G. E. Karniadakis, “NSFnets (Navier-Stokes flow nets): Physics-informed neural networks for the incompressible Navier-Stokes equations,” *Journal of Computational Physics*, vol. 426, p. 109951, feb 2021.
- [46] S. A. Niaki, E. Haghighat, T. Campbell, A. Poursartip, and R. Vaziri, “Physics-Informed Neural Network for Modelling the Thermochemical Curing Process of Composite-Tool Systems During Manufacture,” *Computer Methods in Applied Mechanics and Engineering*, vol. 384, p. 113959, nov 2020.
- [47] Q. Zhu, Z. Liu, and J. Yan, “Machine learning for metal additive manufacturing: predicting temperature and melt pool fluid dynamics using physics-informed neural networks,” *Computational Mechanics*, vol. 67, no. 2, pp. 619–635, 2021.
- [48] G. Kissas, Y. Yang, E. Hwuang, W. R. Witschey, J. A. Detre, and P. Perdikaris, “Machine learning in cardiovascular flows modeling: Predicting arterial blood pressure from non-invasive 4D flow MRI data using physics-informed neural networks,” *Computer Methods in Applied Mechanics and Engineering*, vol. 358, p. 112623, jan 2020.
- [49] N. Wang, H. Chang, and D. Zhang, “Efficient uncertainty quantification for dynamic subsurface flow with surrogate by Theory-guided Neural Network,” *Computer Methods in Applied Mechanics and Engineering*, vol. 373, p. 113492, 2021.
- [50] C. G. Fraces and H. Tchelepi, “Physics informed deep learning for flow and transport in porous media,” *Society of Petroleum Engineers - SPE Reservoir Simulation Conference 2021, RSC 2021*, 2021.
- [51] L. Lu, X. Meng, Z. Mao, and G. E. Karniadakis, “DeepXDE: A deep learning library for solving differential equations,” *SIAM Review*, vol. 63, no. 1, pp. 208–228, 2021.
- [52] O. Hennigh, S. Narasimhan, M. A. Nabian, A. Subramaniam, K. Tangsali, Z. Fang, M. Rietmann, W. Byeon, and S. Choudhry, “NVIDIA SimNet™: An AI-Accelerated Multi-Physics Simulation Framework,” *Lecture Notes in Computer Science (including subseries Lecture Notes in Artificial Intelligence and Lecture Notes in Bioinformatics)*, vol. 12746 LNCS, pp. 447–461, 2021.
- [53] E. Haghighat and R. Juanes, “SciANN: A Keras/TensorFlow wrapper for scientific computations and physics-informed deep learning using artificial neural networks,” *Computer Methods in Applied Mechanics and Engineering*, vol. 373, p. 113552, 2021.
- [54] S. Wang, X. Yu, and P. Perdikaris, “When and why PINNs fail to train: A neural tangent kernel perspective,” *Journal of Computational Physics*, vol. 449, pp. 1–29, 2022.

- [55] S. Wang, H. Wang, and P. Perdikaris, “On the eigenvector bias of Fourier feature networks: From regression to solving multi-scale PDEs with physics-informed neural networks,” *Computer Methods in Applied Mechanics and Engineering*, vol. 384, p. 113938, oct 2021.
- [56] A. D. Jagtap, K. Kawaguchi, and G. E. Karniadakis, “Adaptive activation functions accelerate convergence in deep and physics-informed neural networks,” *Journal of Computational Physics*, vol. 404, p. 109136, 2020.
- [57] M. A. Nabian, R. J. Gladstone, and H. Meidani, “Efficient training of physics-informed neural networks via importance sampling,” *Computer-Aided Civil and Infrastructure Engineering*, pp. 1–16, 2021.
- [58] E. Haghighat, M. Raissi, A. Moure, H. Gomez, and R. Juanes, “A physics-informed deep learning framework for inversion and surrogate modeling in solid mechanics,” *Computer Methods in Applied Mechanics and Engineering*, vol. 379, p. 113741, jun 2021.
- [59] E. Haghighat, A. C. Bekar, E. Madenci, and R. Juanes, “A nonlocal physics-informed deep learning framework using the peridynamic differential operator,” *Computer Methods in Applied Mechanics and Engineering*, vol. 385, p. 114012, nov 2021.
- [60] E. Samaniego, C. Anitescu, S. Goswami, V. M. Nguyen-Thanh, H. Guo, K. Hamdia, X. Zhuang, and T. Rabczuk, “An energy approach to the solution of partial differential equations in computational mechanics via machine learning: Concepts, implementation and applications,” *Computer Methods in Applied Mechanics and Engineering*, vol. 362, p. 112790, 2020.
- [61] V. M. Nguyen-Thanh, X. Zhuang, and T. Rabczuk, “A deep energy method for finite deformation hyperelasticity,” *European Journal of Mechanics, A/Solids*, vol. 80, p. 103874, 2020.
- [62] W. Li, M. Z. Bazant, and J. Zhu, “A physics-guided neural network framework for elastic plates: Comparison of governing equations-based and energy-based approaches,” *Computer Methods in Applied Mechanics and Engineering*, vol. 383, p. 113933, sep 2021.
- [63] B. Moseley, A. Markham, and T. Nissen-Meyer, “Finite Basis Physics-Informed Neural Networks (FBPINNs): a scalable domain decomposition approach for solving differential equations,” *arXiv*, 2021.
- [64] S. Wang, Y. Teng, and P. Perdikaris, “Understanding and mitigating gradient flow pathologies in physics-informed neural networks,” *SIAM Journal on Scientific Computing*, vol. 43, no. 5, pp. 3055–3081, 2021.

- [65] B. Bahmani and W. Sun, “Training multi-objective/multi-task collocation physics-informed neural network with student/teachers transfer learnings,” *arXiv*, 2021.
- [66] E. Haghighat, D. Amini, and R. Juanes, “Physics-informed neural network simulation of multiphase poroelasticity using stress-split sequential training,” *arXiv*, 2021.
- [67] R. Cipolla, Y. Gal, and A. Kendall, “Multi-task Learning Using Uncertainty to Weigh Losses for Scene Geometry and Semantics,” *Proceedings of the IEEE Computer Society Conference on Computer Vision and Pattern Recognition*, pp. 7482–7491, 2018.
- [68] A. Paszke, S. Gross, F. Massa, A. Lerer, J. Bradbury, G. Chanan, T. Killeen, Z. Lin, N. Gimelshein, L. Antiga, A. Desmaison, A. Köpf, E. Yang, Z. DeVito, M. Raison, A. Tejani, S. Chilamkurthy, B. Steiner, L. Fang, J. Bai, and S. Chintala, “PyTorch: An imperative style, high-performance deep learning library,” *Advances in Neural Information Processing Systems*, vol. 32, no. NeurIPS, 2019.
- [69] H. P. Langtangen and G. K. Pedersen, *Scaling of Differential Equations*. Springer Cham, 2016.
- [70] C. Ozturk and E. Simdi, “Geostatistical investigation of geotechnical and constructional properties in kadikoy–kartal subway, turkey,” *Tunneling and Underground Space Technology*, vol. 41, pp. 35–45, 2014.
- [71] F. Tinti, D. Boldini, M. Ferrari, M. Lanconelli, S. Kasmaee, R. Bruno, H. Egger, A. Voza, and R. Zurlo, “Exploitation of geothermal energy using tunnel lining technology in a mountain environment. a feasibility study for the brenner base tunnel – bbt,” *Tunneling and Underground Space Technology*, vol. 70, pp. 182–203, 2017.
- [72] Y. Zhang, W. Ji, D. D. Saurette, T. H. Easher, H. Li, Z. Shi, V. I. Adamchuk, and A. Biswas, “Three-dimensional digital soil mapping of multiple soil properties at a field-scale using regression kriging,” *Geoderma*, vol. 366, p. 114253, 2020.
- [73] N. Cressie, *Statistics for Spatial Data*. Wiley, 1993.
- [74] J. Davis, *Statistics and data analysis in Geology*. Wiley, 2002.
- [75] S. J. Pan and Q. Yang, “A survey on transfer learning,” *IEEE Transactions on knowledge and data engineering*, vol. 22, no. 10, pp. 1345–1359, 2009.
- [76] S. Goswami, C. Anitescu, S. Chakraborty, and T. Rabczuk, “Transfer learning enhanced physics informed neural network for phase-field modeling of fracture,” *Theoretical and Applied Fracture Mechanics*, vol. 106, no. November 2019, p. 102447, 2020.
- [77] S. Chakraborty, “Transfer learning based multi-fidelity physics informed deep neural network,” *Journal of Computational Physics*, vol. 426, p. 109942, 2021.

- [78] D. P. Kingma and J. L. Ba, “Adam: A method for stochastic optimization,” in *3rd International Conference on Learning Representations, ICLR 2015 - Conference Track Proceedings*, 2015.
- [79] C. Bajaj, L. McLennan, T. Andeen, and A. Roy, “Robust Learning of Physics Informed Neural Networks,” *arXiv*, pp. 1–20, 2021.
- [80] A. S. Krishnapriyan, A. Gholami, S. Zhe, R. Kirby, and M. W. Mahoney, “Characterizing possible failure modes in physics-informed neural networks,” *Advances in Neural Information Processing Systems*, vol. 34, 2021.